1

Two-Terminal Neuromorphic Memristors

Hui-Kai He, He-Ming Huang, and Rui Yang

Huazhong University of Science and Technology, School of Materials Science and Engineering, Wuhan 430074, P. R. China

1.1 Memristive Devices

A memristive device is a resistive device with an inherent memory; its theory was creatively conceived by Prof. Chua in 1971 [1] and was connected to the physical devices in 2008 by HP [2]. Since then, memristive devices have been extensively studied over the past decade due to their prominent advantages, such as simple structure, high operation speed, and low power consumption in applications of data storage, logic operation, and neuromorphic computation [3]. In this section, we will introduce traditional two-terminal memristive devices, mainly focusing on device structure and memristive materials.

1.1.1 Memristive Device Structure and Materials

1.1.1.1 Memristive Device Structure

Typically, a memristive device has a metal/insulator/metal (MIM) structure, composed of a switching layer sandwiched between two metal electrodes (possibly different), as shown in Figure 1.1a. Because of its simple structure, highly scalable cross-point and multilevel stacking memory structures have been proposed (Figure 1.1b), which is promising for the construction of huge neural networks and neuromorphic computing systems [3]. It is well known that electrodes play a crucial role in the resistive switching behavior of memristive devices. To date, in addition to metals (such as Ag [5], Cu [6], Pt [7], Au [8], Al [9], and W [10]), a variety of conductive materials have been explored as electrodes for memristors, including nitrides such as TiN [11], carbon materials such as graphene [12] and carbon nanotubes [13], conductive oxides such as ITO [14] and $SrRuO_3$ (SRO) [15], p- and n-type Si [16], and so on. Among these metals, Ag and Cu are the most popular ones due to their ability to dissolve in thin film electrolyte at low electric field and their high ionic mobility [17]. In addition to the electrodes, the switching layer where the resistive switching takes place is the key layer in memristive devices and has a great

Neuromorphic Devices for Brain-Inspired Computing: Artificial Intelligence, Perception, and Robotics, First Edition. Edited by Qing Wan and Yi Shi.

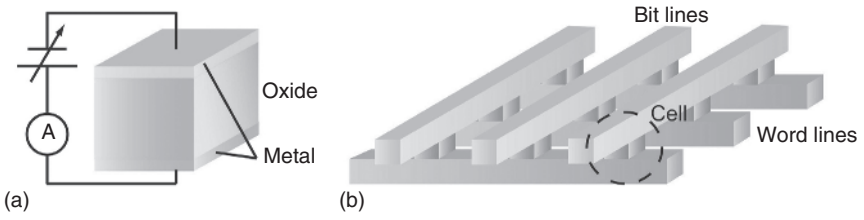

Figure 1.1 (a) Diagram of a memristive device with a capacitor-like structure in which a switching layer is sandwiched between two metal electrodes. (b) Diagram of a cross-point memory structure. Word and bit lines are used for selecting a memristive device and writing/reading data, respectively. Source: Sawa [4].

impact on the device performance. Typically, the switching layer is an insulator or a semiconductor. Also, it is normally in the form of thin film, which is compatible to large-scale integration in the semiconductor industry. Recently, other forms of the switching layer are also intensively investigated, including nanoparticles [18], nanowires [19], two-dimensional (2D) materials [20], three-dimensional nanoarrays, etc. Note that we mainly discuss memristors in the form of thin film in all below sections.

1.1.1.2 Memristive Materials

As mentioned above, the materials involved in memristors include switching materials and electrode materials. Here, we mainly focus on switching materials, which is also termed as memristive materials. Up to now, a great number of memristive materials have been explored for memristive devices used in neuromorphic computing. In this chapter, the memristive materials are subdivided into inorganic and organic materials. Generally speaking, inorganic materials have significant advantages over organic ones in switching stability and manufacturing technology, while organic ones stand out in terms of high-mechanical flexibility and low cost.

Inorganic materials for memristors can be loosely divided into binary oxides (e.g. TiO_x [21], TaO_x [22], HfO_x [23], WO_x [24], and ZnO [14]), perovskite oxides (e.g. $SrTiO_3$ [25] and $BiFeO_3$ [26]), and 2D materials (e.g. graphene [27], hexagonal boron nitride (h-BN) [28], and molybdenum disulfide (MoS_2) [20]). Among these inorganic materials, binary oxides have been intensively studied since they are the most abundant and show superior switching characteristics including ultrahigh ON/OFF ratio, sub-ns operation speed, and extreme endurance. In addition, their simple composition enables them to be easily fabricated by various film deposition technologies, mainly including magnetron sputtering [14, 24], atomic layer deposition (ALD) [29], thermal oxidation [30], and plasma oxidation [11]. Magnetron sputtering is a high-rate, high-efficient film deposition technology and is becoming increasingly popular owing its high-yield and low-cost production of uniform films over large areas. Recently, ALD has also attracted increasing attention for the deposition of binary oxides due to its ability to accurately control the thickness and uniformity of the films. Furthermore, binary oxides have good compatibility with conventional complementary metal oxide semiconductor (CMOS) process and good thermal stability. Thus, binary oxides have been the focus of both academic

and industrial communities over the past decade. In particular, research interest in HfO_x and TaO_x has been extremely high in the past few years since they exhibit both sub-ns operation speed and extreme endurance of $>10^{10}$ cycles and may be the most promising memristive materials for practical applications in the near future.

In addition to binary oxide, perovskite oxides such as $SrTiO_3$, $SmNiO_3$, $BiFeO_3$, and $SrRuO_3$ have also been researched for memristors over the past few years. Among these perovskite oxides, $SrTiO_3$ receives the most attention for the implementation of memristive synapses because of its superior memristive properties and rich switching dynamics [25, 31, 32]. It has been found that perovskite oxides have advantages of excellent localized accumulation of oxygen ions and can be easily converted into a defective structure. However, it should be mentioned that they are generally obtained through pulsed laser deposition (PLD) under high temperature. Although this is an advanced deposition method that can obtain high-quality thin films with accurate stoichiometry, it is not widely used in the semiconductor industry due to its high-cost and the small uniform area of the deposited film, greatly hindering the development and application of perovskite oxides in memristors.

In recent years, 2D materials have become a new focus in memristors for the realization of artificial synapses and neurons due to their superior physical, chemical, and mechanical properties, including graphene, MoS_2, and h-BN. Graphene is one of the highly desirable materials for memristive bioinspired devices owing to its excellent properties of low cost, tunability, nontoxicity, flexibility, and biocompatibility [33, 34]. However, graphene is inherently a semimetallic material and needs to be oxidized or doped when it is used as a switching layer. In contrast to graphene, transition metal chalcogenides (TMDs), such as MoS_2 and tungsten selenide (WSe_2), are semiconductors with proper bandgaps from 1 to 2 eV [35]. Therefore, TMDs are considered as ideal substitutes for graphene. MoS_2, the common member of the TMDs family, has been intensively investigated and shows superior performance including ultrahigh ON/OFF ratio [36], ultralow operating voltage [37], and excellent thermal stability [38]. Reliable production of 2D materials with uniform properties is essential for translating their new electronic and optical properties into applications. Until now, various fabrication methods including mechanical exfoliation [39], liquid-phase exfoliation [40], and chemical vapor deposition (CVD)[41] have been employed to obtain atomically thin flakes of 2D materials. First discovered by Novoselov et al. in 2004, ultrathin 2D materials are peeled from their parent bulk crystals by mechanical exfoliation using adhesive tape. This method produces single-crystal flakes of high purity and cleanliness that are suitable for fundamental characterization. Liquid-phase exfoliation method is also a feasible way to prepare atomically thin 2D material. It can produce gram quantities of submicrometer-sized monolayers, but the resulting exfoliated material differs structurally and electronically from the bulk material [42]. To obtain large-area and uniform layers, CVD method is very promising. Such methods give reasonably good-quality material with typical flake sizes of hundreds of nanometers to a few centimeters, although the flake thickness is not conclusively shown to be monolayers.

Compared with inorganic materials, organic materials have the advantages of low cost, ease of fabrication, and, especially, high-mechanical flexibility. In

addition, it is easy to modulate the electrical performance of organic materials by a designed molecular synthesis [43]. Accordingly, organic materials are attracting more and more attention that enable them to be promising for future flexible electronics, although most switching characteristics of organic materials are still not comparable with those of inorganic materials. It is well known that organic materials consist of large molecules with long chains of repeating monomer units. Hence, solution processes, for example, spin coating, are normally adopted to prepare organic films [44, 45]. Note that organic materials still suffer from some problems like poor thermal stability and bad compatibility with CMOS process [46].

1.1.2 Resistive Switching Behavior

The intrinsic physical phenomenon behind memristive devices is resistive switching (RS), which means the resistance can be reversely changed between low resistive state (LRS) and high resistive state (HRS) under external electric stimuli, resulting in a pinched hysteresis current–voltage (I–V) loop. If the resistance state of the memristive device changes from HRS to LRS, it is called an SET operation and is also considered as a "write" process. In contrast, if the resistance state is converted from LRS to HRS, it is called RESET operation and means an "erase" process (Figure 1.2).

Actually, the switching behavior can be classified into different types on the basis of I–V characteristics according to different criteria. Based on the polarity of the external electric field, the switching behaviors can be classified into two types: unipolar and bipolar resistive switching. The unipolar switching operates independently of the voltage polarity, which is also named nonpolar switching sometimes. Meanwhile, the bipolar switching shows a directional resistive switching, depending on the polarity of the applied voltage. On the basis of the switching dynamics, the switching behavior can be classified into digital and analog types. Generally, the digital resistive switching shows abrupt current jumping in the I–V curves, while the analog switching has continuous current curve during voltage sweeping. Digital resistive switching is preferable in the information storage because of its high ON/OFF ratio and fast switching speed [48, 49]. In contrast, the analog resistive switching is particularly concerned for artificial synaptic devices, since the gradual change of the resistance well resembles the potentiation/inhabitation of the synaptic weight in the adaptive learning process of a synapse [50]. The switching behaviors in Figure 1.2b,d are generally nonvolatile and widely used in the application of data storage. Notably, the analog switching shown in Figure 1.2c is usually nonvolatile but sometimes is volatile with current decay effect. The volatile analog switching with versatile time constants is desirable for simulating short-term and long-term synaptic plasticity. The unipolar digital switching shown in Figure 1.2a is volatile and is usually named as threshold switching, in which the device switches to LRS upon the application of a certain threshold voltage and then spontaneously decays back to HRS after the removal of the external voltage. This threshold switching is promising for implementing the threshold firing process of the neuron. Below, we mainly focus on the volatile and nonvolatile resistive switching.

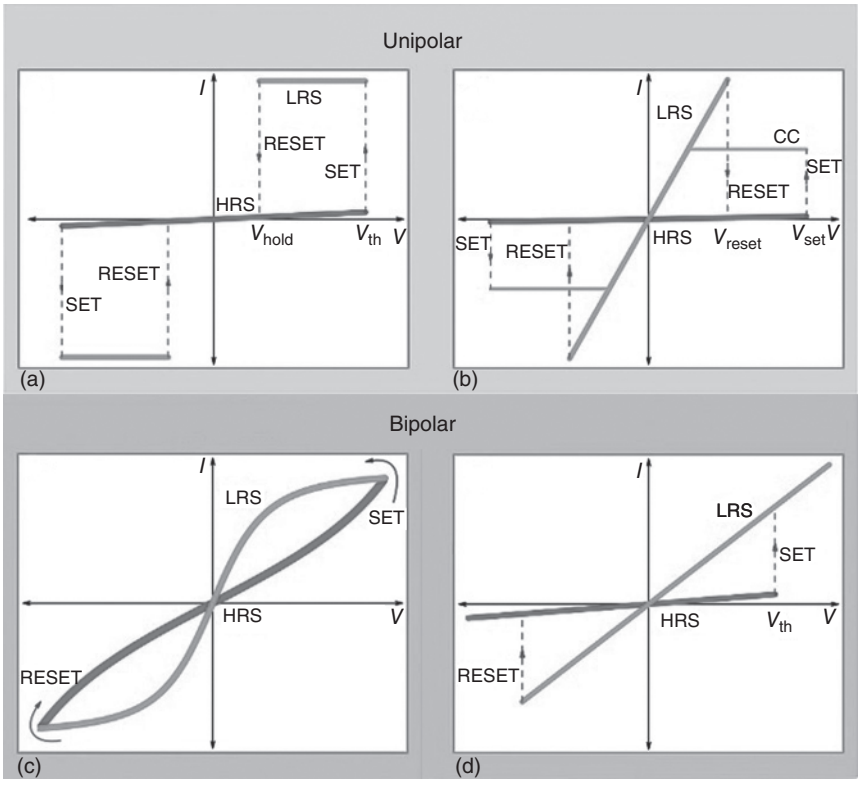

Figure 1.2 Typical *I*–*V* characteristics for different switching behaviors in memristive devices. (a) Unipolar threshold switching. (b) Unipolar digital switching with nonvolatility. (c) Bipolar analog switching with tunable volatility. (d) Bipolar digital switching with nonvolatility. Source: Yang et al. [47].

1.1.2.1 Volatile Resistive Switching

The current of the memristive device showing spontaneously decay after the removal of the external electric field is termed as volatile resistive switching, including volatile analog switching and threshold switching. Both of them can be utilized in the construction of artificial synapses and neurons.

To date, volatile analog switching has been observed in a variety of materials, such as WO_x [24], $Pr_{0.7}Ca_{0.3}MnO_3$ (PCMO) [51], and Nb-$SrTiO_3$ [11]. Moreover, it has been found that this switching is generally based on interface-type resistive switching, which will be discussed later. Note that the decay characteristics are essential in the emulation of both short- and long-term plasticity of biological synapses. Thus, we next give a brief introduction to the dynamic process of volatile analog switching using the Pd/WO_x/W memristor as an example [30]. After the stimulation of write pulses, current decay process of the device is carefully monitored by small read pulses, as shown in Figure 1.3a. The stimulation drives the current higher; however after the stimulation is removed, the current decreases with time. One can see that the decay appears to occur at two different time scales: right after stimulation, the

current shows a very fast decay, and the decay becomes much slower after several seconds. Then, the decay can be well fitted by the sum of two stretched exponential functions with two time constants: a short-term effect with time constant ≈52.5 ms and a long-term time constant ≈92.5 seconds:

$$I = A_1 \times I_{\text{short}} + A_2 \times \mathrm{I}_{\text{long}} = A_1 \mathrm{I}_{0s} \exp\left[-\left(\frac{t}{\tau_s}\right)^{\beta_s}\right] + A_2 I_{01} \exp\left[-\left(\frac{t}{\tau_1}\right)^{\beta_1}\right]$$

where τ_s (τ_1), I_{0s} (I_{01}), and β_s (β_1) are the characteristic relaxation time, prefactor, and stretch index for the short-term (long-term term) process, respectively. Borrowing terms used in neuroscience, the first stage with time constant ≈52.5 ms is considered short-term, and the second stage with time constant ≈92.5 seconds is considered long-term. These two time constants differ by more than 3 orders of magnitude, which enable the memristor to emulate important rate- and timing-dependent behaviors at both short term and long term.

In addition to volatile analog switching, threshold switching is also volatile, and the current will decay over time once the applied voltage or pulse is removed. Recently, threshold switching was demonstrated by Wang et al. in two-terminal diffusive memristors based on Ag-doped SiO_xN_y [52]. Also, the decay process was attributed to the spontaneous rupture of the Ag filament driven by minimization of the interfacial energy between Ag and the dielectric after removing the external electric field. Figure 1.3b displays decay characteristics of the SiO_xN_y:Ag diffusive memristor showing variation of current (open circle) with applied voltage pulses (solid line). Under an applied pulse, the device exhibits threshold switching to an LRS after an incubation period (delay time). This delay time is related to the growth and clustering of silver nanoparticles to eventually form conduction channels. Following channel formation, the current jumps abruptly by several orders of magnitude and then slowly increases further under bias as the channel thickens. Once the voltage pulse is removed, the device relaxes back to its original HRS over

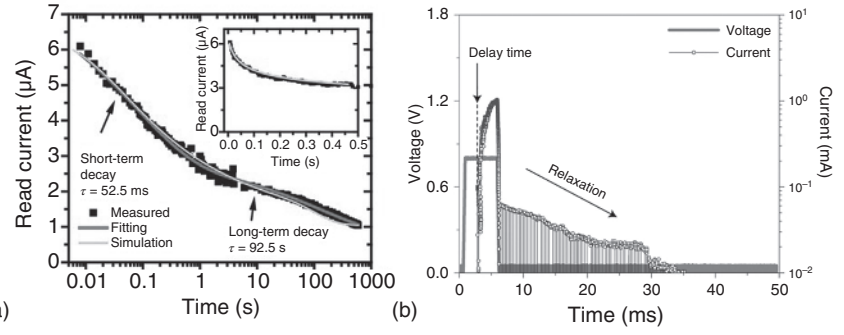

Figure 1.3 Decay characteristics of volatile analog switching and threshold switching devices. (a) Current decay of the Pd/WO_x/W device after the removal of the applied voltage pulses. The experimental data (black squares) can be fitted by the sum of two stretched exponential functions with distinct relaxation time constants. Source: Du et al. [30]. (b) Decay characteristics of the SiO_xN_y:Ag diffusive device showing variation of current (open circles) with applied voltage pulses. Source: Wang et al. [52].

a characteristic time (relaxation time). More importantly, the relaxation time is on the same order as the response of bio-synapses, that is, tens of milliseconds. Furthermore, it has been demonstrated that the relaxation time is related to the temperature, the voltage pulse parameters, operation history, Ag concentration, host lattice, device geometry, and humidity, which alone or in combination can be used to tune the desired dynamics for neuromorphic systems.

1.1.2.2 Nonvolatile Resistive Switching

Unlike volatile resistive switching, nonvolatile resistive switching, including bipolar digital switching and nonvolatile analog switching, means that the conductance is maintained after the removal of the external electric field. For bipolar digital switching, the device abruptly changes to LRS upon the application of a positive (negative) threshold voltage and then returns to HRS upon the application of a negative (positive) threshold voltage. Such switching is preferable in data storage due to its high ON/OFF ratio, fast switching speed, and long retention. Recently, thanks to high scalability and large dynamic range, this switching has also been used in memristors for the construction of artificial synapses [53, 54]. However, one disadvantage of this switching is the limited number of conductance states and low conductance update linearity, highly hindering its application and development in neuromorphic computing.

In contrast, nonvolatile analog switching, with multilevel conductance states and high conductance update linearity, has recently attracted increasing attention in the construction of neural network accelerators and neuromorphic systems. On the basis of the nonvolatile analog switching, vector–matrix multiplication (VMM) or weighted summation operation can be physically implemented in a cross-bar array of memristive devices based on Ohm and Kirchhoff laws [55, 56]. In this case, the VMM operation can be accelerated in a parallel, in-memory, and analog manner in the memristor crossbar, which could largely benefit data-centric and VMM-intensive algorithms, including a large majority of artificial neural network (ANN) algorithms and many other arithmetic calculations. This part will be introduced in detail in Section 1.5.

1.2 Resistive Switching Mechanisms

In the past few years, the switching mechanisms of memristors have been vigorously investigated to predict and manipulate the switching profiles to achieve superior switching performance [49, 57]. Especially for artificial synapses and neurons, the required characteristics are broadened to work sensitively to the input stimulus and generate controllable conductance change [58]. To closely mimic biological synapses and neurons, regulating the conductance change of the memristive device under electric stimuli becomes extremely important. Therefore, it is necessary for us to have a deep understanding of the switching mechanisms of memristors. Here, the common switching mechanisms are classified into two types including filamentary-type resistive switching and interface-type resistive switching according to the position where the resistive switching occurs.

1.2.1 Filamentary-Type Resistive Switching

In a memristive device base on the filamentary-type resistive switching, a forming process is usually required to obtain stable resistive switching behavior, during which conductive filaments (CFs) form and the memristive device reaches a LRS. Subsequently, local rupture and re-formation of the CFs occur during the reset and set processes, respectively, resulting in the alternation between HRS and LRS. Accordingly, the resistance value of LRS exhibits no or weak dependence on the device size in filamentary-type memristive devices [49]. Generally, the growth and rupture of CFs results from ion migration. Based on the polarities of the charges, there are two types of ions: cations and anions in nature, and they migrate in opposite directions under an external electric field. Thus, the filamentary-type resistive switching can be subdivided into cation migration-related filaments and anion migration-related filaments, and growth and rupture processes of the CFs based on each of these are discussed separately as follows.

1.2.1.1 Cation Migration-Related Filaments

The cation migration-based memristive devices typically have an electrochemically active electrode (AE), such as Ag or Cu; an electrochemically inert counter electrode (CE), such as Pt, Au, or W; and a thin film of a solid electrolyte, such as Ag^+ or Cu^+ ion conductor, sandwiched between both electrodes [59]. The CFs are formed via electrochemical dissolution and then redeposition of the active metal atoms. Therefore, such memristive devices are often called electrochemical metallization cells (ECM) and are also referred to programmable metallization cells (PMCs) or atomic switches in some literatures [60–62]. The first observation of a metal filament in ECM was achieved by Hirose in 1976. [63]. They demonstrated nonvolatile resistive switching behavior in the Ag/Ag–As_2S_3/Mo sandwich device. To clarify the switching mechanism, a planar Ag/Ag–As_2S_3/Au device was fabricated at the same time, and the growth of Ag filaments from the CE (Au electrode) to the AE (Ag electrode) was confirmed by optical microscopy.

The resistive switching process of an ECM device with Cu as the AE and Pt as the CE is schematically shown in Figure 1.4. The overall switching process consists of the following steps: (a) Upon applying a high enough positive voltage to Cu, metallic Cu is oxidized to Cu^+ ions in accordance with the reaction, $Cu \rightarrow Cu^+ + e^-$. (b) Cu^+ ions migrate along fast diffusion channels toward the CE driven by external electric field, and Cu^+ ions are reduced back to metallic Cu according to the reaction, $Cu^+ + e^- \rightarrow Cu$. (c) The Cu filament continues to grow, and two electrodes become connected. As a result, the ECM device switches from HRS to LRS. (d) Under negative voltage, the Cu filaments can be electrochemically dissolved with the help of Joule heating, thereby resetting the ECM device back to the HRS.

Although there is no doubt about the presence of metal filaments in cation migration-based memristors, the direct observation of metal filaments, especially their dynamic growth and rupture processes, has attracted great interest in academia. Originally, only ex situ observations of metal filaments in planar microscale ECM cells were reported. In recent years, thanks to advances in fabrication and characterization of nanomaterials, both ex situ and in situ observations

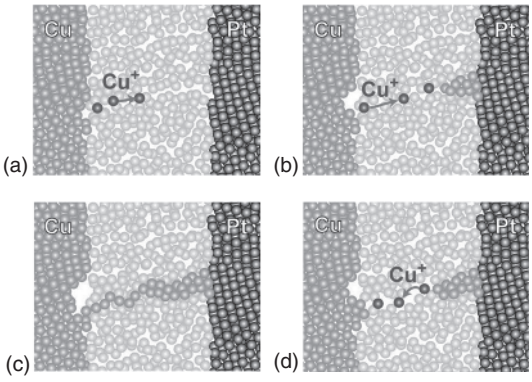

Figure 1.4 Schematic presentation of the resistive switching processes of an ECM device with Cu as the AE and Pt as the CE. (a) forming process, (b) SET process, (c) ON state, (d) RESET process. Source: Zidan et al. [64].

of metal filaments in vertical nanoscale ECM cells have been extensively explored. In 2012, Yang et al. reported the formation/rupture of nanoscale Ag filaments in $Ag/SiO_2/Pt$ device by transmission electron microscopy (TEM) technique [65]. After application of a positive voltage bias to the Ag electrode, the as-fabricated device was switched to the LRS with an abrupt increase in current, as shown in Figure 1.5c. The electrical resistance change was found to accompany changes in the electrode and the switching material (Figure 1.5a), where Ag was injected into the insulating SiO_2 layer and the two electrodes were connected by the Ag

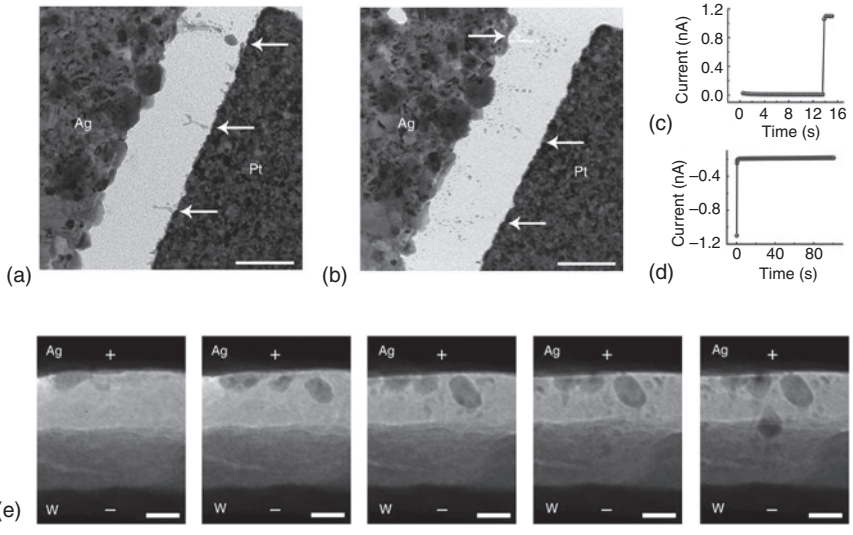

Figure 1.5 (a) TEM image of the $Ag/SiO_2/Pt$ device after the forming process. Scale bar: 200 nm. (b) TEM image of the same device after erasing. Scale bar: 200 nm. (c) Corresponding *I*–*t* curve during the forming process that led to the image in (a). The applied voltage was 8 V. (d) Corresponding *I*–*t* curve during the erasing process that led to the image in (b). The applied voltage was −10 V. (e) Real-time structural evolutions of an Ag/a-Si/W-based device obtained through in situ TEM observation, showing the dynamic filament growth process that initiates from the reactive electrode. Source: Yang et al. [65].

filaments. Upon voltage bias of opposite polarity, the device switched back to the HRS (Figure 1.5d), corresponding to the rupture of the Ag filaments (Figure 1.5b). These observations unambiguously reveal the physical nature of the resistive switching process, where the physically displaced Ag atoms lead to the dramatic changes to the device's electrical properties. Besides direct observation of the metal filaments during resistive switching by ex situ TEM, in situ TEM technique provides important information concerning the microscopic dynamic ionic processes during filament growth. In Yang's work, the filament growth was further demonstrated in vertical Ag/a–Si/W ECM device via in situ TEM observation, as shown in Figure 1.5e. One can identify the real-time structural evolution of the ECM device since the filament growth is directly related to the electric measurements. The systematic in situ TEM analyses offers a complete picture of the different dynamic processes that occur in the ECM device, e.g. filament growth direction, position, and morphology [66].

Notably, the filament growth/dissolution dynamics can be affected by the ionic mobility and the redox reaction rate. Therefore, the filament dynamics can be classified into four categories (Figure 1.6). (i) In the case of high ion mobility and high redox rate, the ions can reach the inert electrode without agglomerating, thus avoiding nucleation within the insulating film so filament growth initiates from the inert electrode, and the large amount of ion supply due to high redox rate leads to the formation of cone-shaped filaments with its base at the inert electrode interface as shown in Figure 1.6a. Such case can be found in ECM devices with traditional solid electrolytes such as GeTe [67] that are known to be good ionic conductors. (ii) In the

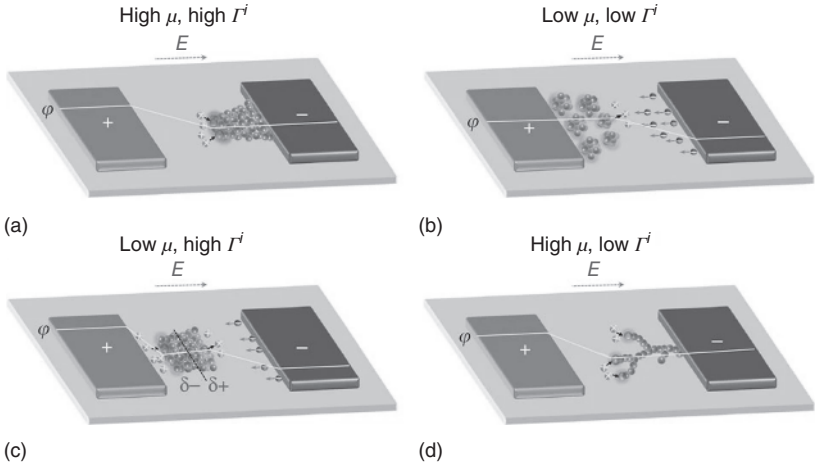

Figure 1.6 (a) Both ion mobility and redox rate are high, resulting in the filament growth from the inert electrode and an inverted cone shape. (b) Both ion mobility and redox rate are low, resulting in the filament growth from the active electrode with discrete nanoclusters and a forward cone shape. (c) Ion mobility is low, but redox rate is high, resulting in the filament nucleation inside the dielectric and reconnection with the source. (d) Ion mobility is high, but redox rate is low, resulting in the filament growth from the inert electrode and a branched structure. Source: Yang et al. [66].

case of low ion mobility and low redox rate (Figure 1.6b), the ions can pile and reach the critical nucleation conditions inside the dielectric, and further filament growth is fulfilled by cluster displacement via the repeated splitting–merging processes. An experimental example is the filament growth in amorphous Si, where the filament is initiated from the active electrode and grows toward the inert electrode as discrete nanoclusters [68]. (iii) In the case of low ion mobility and high redox rate, nucleation can occur inside the dielectric while large amounts of atoms can be deposited onto the cathode sides of the nuclei, leading to the gap filling shown in Figure 1.6c. (iv) In the case of high ion mobility and low redox rate (Figure 1.6d), nucleation only occurs at the inert electrode, but the limited ion supply means that the reduction predominately occurs at the edges with high field strengths, thus leading to the branched filament growth toward the active electrode.

Ion mobility and redox rate can be tuned by the careful selection of the electrode material and the switching materials, as well as the operating conditions since both can be strongly affected by the applied electric field and temperature. Hence, it is possible to adjust the filament dynamics by selecting proper electrode material, switching materials, and operating conditions. The behavior and characteristics of filament are important for artificial synapses and neurons because the filament dynamics is closely related to the synaptic plasticity.

1.2.1.2 Anion Migration-Related Filaments

Besides metal ions, the redox and migration processes of anions, mostly oxygen ions, are involved in the memristive devices based on transition metal oxides without electrochemical active electrodes. The migration of oxygen ions usually induces a redox reaction expressed by a valence change of the cation sublattice and leads to a stoichiometry change of the oxides. Therefore, anion migration-related filament mechanism is typically named as valence change mechanism (VCM). In a VCM device, resistive switching generally relies on the creation and annihilation of oxygen-deficient (or oxygen vacancies, $V_O^{\cdot\cdot}$) CFs based on oxygen migration. In contrast to ECM devices, VCM devices generally consist of inert electrodes and the switching materials. The switching layer is normally a transition metal oxide such as binary metal oxides and ternary perovskite oxide.

The switching process of a VCM device with inert electrodes and a transition metal oxide is schematically shown in Figure 1.7. $V_O^{\cdot\cdot}$ are randomly distributed at the initial state (Figure 1.7a). When the top electrode (TE) is positively biased, $V_O^{\cdot\cdot}$ migrate toward the bottom electrode (BE) and accumulate in the oxide/BE interface (Figure 1.7b). Afterward, $V_O^{\cdot\cdot}$ continue to accumulate under the positive voltage bias. Once the $V_O^{\cdot\cdot}$ CFs form and connect the TE and BE, the device switches into the LRS (Figure 1.7c). With the growth mode from the BE to the TE, the thinnest part of the formed CF should be located near the TE. When the TE is negatively biased, Joule heat is mainly concentrated on the thinnest part of the CF, and $V_O^{\cdot\cdot}$ in this region migrate toward the TE and then is replaced by the oxygen ions. As a result, the concentration of $V_O^{\cdot\cdot}$ in the thinnest part of the CF will be significantly decreased, leading to the rupture of the CF at that location (Figure 1.7d).

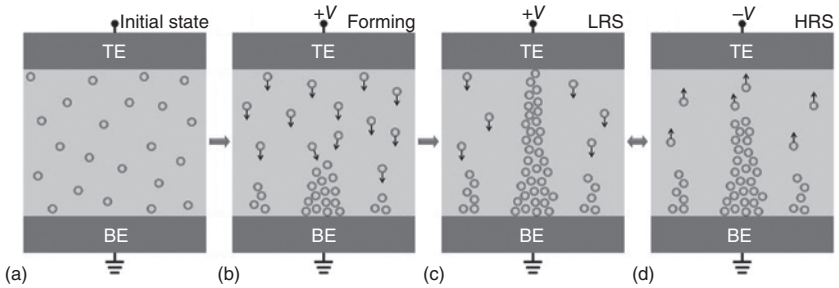

Figure 1.7 Schematic presentation of the switching process of a VCM device with inert electrodes and a transition metal oxide. (a) The initial state with randomly distributed $V_O^{\cdot\cdot}$. (b) The nucleation and subsequent growth from cathode to anode of $V_O^{\cdot\cdot}$ filament during forming process. (c) The LRS with a complete filament whose thinnest region is near the anode. (d) The HRS with a partially ruptured filament at its thinnest region. Source: Pan et al. [48].

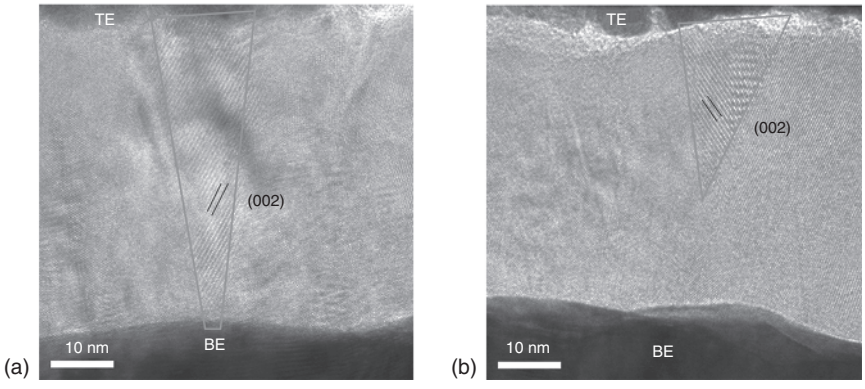

Figure 1.8 (a) High-resolution TEM image of a V_O nanofilament in Pt/TiO_2/Pt device after the set operation. (b) High-resolution TEM image of an incomplete filament in the same device after the reset operation. Source: Kwon et al. [68].

Similar to ECM devices, a host of material characterization techniques such as TEM and spectroscopic analysis have recently been employed to reveal the microscopic origin of resistive switching behaviors in VCM devices. Figure 1.8 shows high-resolution TEM (HRTEM) image of the same location in a Pt/TiO_2/Pt device after applying negative (set) and positive (reset) voltages, respectively [68]. Clear contrast differences in the HRTEM images can be observed, indicating changes in the composition of the film at different resistance states. In the set sample (Figure 1.8a), a connected V_O filament in the conical shape (marked by a gray line) was found between top electrode and bottom electrode. After the reset operation (Figure 1.8b), the connected filament ruptured and an incomplete filament was present near the top electrode, verifying the role of V_O migration during the resistive switching process of VCM devices.

It is generally more challenging to directly observe the V_O migration process and filament evolution in VCM devices since the filaments consist of native defects, i.e. $V_{\ddot{O}}$ rather than foreign metallic species. Careful spectroscopic analysis is typically required to confirm the composition changes. Various state-of-the-art techniques such as X-ray absorption spectroscopy (XAS) [69, 70] and photoemission electron microscopy (PEEM) [71, 72] have recently been employed to comprehensively characterize the changes in film microstructure, composition, and chemical states accompanying the resistive switching process in VCM devices.

XAS Analysis Spatially resolved XAS using scanning transmission X-ray microscope (STXM) was performed to nondestructively investigate the chemical and structural changes during resistive switching. Figure 1.9a,b shows the presence of three distinct states of the TiO_2 within the junction area taken at an X-ray energy of 460.0 eV in the Ti L_3-edge in a Pt/TiO_2/Pt device after electroforming and set/reset cycling [69]. Region is outside of the junction area and is most similar to the as-deposited TiO_2, which is known from X-ray diffraction (XRD) to be an amorphous phase. Within the junction (region ii), the spectrum strongly matches the known XAS for anatase, one of the crystalline polymorphs of TiO_2. The altered absorption spectrum in region iii matches that of reduced titanium oxide, in which the valence state of the Ti ions is reduced from +4 to +3. Furthermore, electron diffraction measurement revealed that the region iii is composed of the Ti_4O_7 phase with metallic conductivity, which proves the formation of localized conductive filament due to the migration of $V_{\ddot{O}}$. Thermally driven radial migration of $V_{\ddot{O}}$ was also demonstrated by in operando X-ray absorption spectromicroscopy in a Ta_2O_5-based device (Figure 1.9c,d) [70]. After 10^5

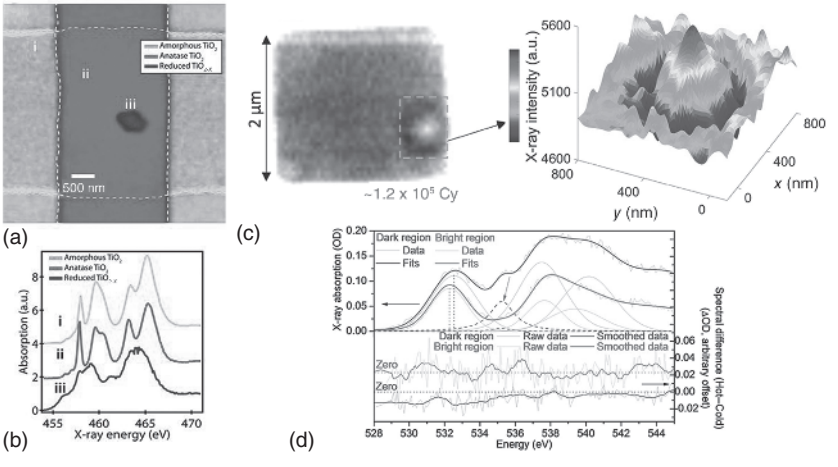

Figure 1.9 (a) Scanning transmission X-ray microscopy (STXM) image of a TiO_2-based device after electrical cycling, showing structural changes and the formation of a localized channel. (b) Corresponding Ti L-edge X-ray absorption spectra from the three regions in panel (a). Source: (a, b) Strachan et al. [69]. (c) O K-edge transmission intensity map of a Ta_2O_5-based device cycled to 120 000 cycles imaged at an energy of 531.2 eV. (d) 3D color intensity plot of the ring seen in (c), displaying the profile of the ring. Source: (c, d) Kumar et al. [70].

cycles, a ring-like feature with a bright inner core and a dark perimeter was observed as shown in Figure 1.9c. In addition to field driven drift of $V_O^{\cdot\cdot}$ in the vertical direction, temperature gradients due to Joule heating near the localized conduction channels produce thermophoretic forces that cause lateral migration of $V_O^{\cdot\cdot}$. As a result, lateral segregation of oxygen-deficient and oxygen-rich regions occurs, corresponding to the bright and dark regions in Figure 1.9c.

X-ray PEEM analysis In operando X-ray PEEM (XPEEM) analysis is a desirable technique to nondestructively reveal the changes in film microstructure, composition, and chemical states during the resistive switching process with high spatial resolution and interface or surface sensitivity. Recently, quantitative redox reactions were demonstrated via in operando XPEEM analysis in a $SrTiO_3$-based device with a graphene top electrode that offers excellent electrical conductivity and photoelectron transparency to allow electrical programming and spectromicroscopy measurements [71]. Noticeable changes were observed in the normalized intensity of O K-edge when the device alternated between the HRS and LRS, indicating the formation and dissolution of the $V_O^{\cdot\cdot}$ filament (Figure 1.10). Furthermore, quantitative information on the charge-carrier density differences between different resistance states is available since XPEEM is a highly surface-sensitive technique.

1.2.2 Interface-Type Resistive Switching

In contrast to the filamentary-type resistive switching, interface-type resistive switching generally originates from the variation of the Schottky barrier caused by migration of $V_O^{\cdot\cdot}$ [73]. In this case, the resistance in the LRS is inversely proportional to the electrode area, suggesting the entire electrode area is involved in the switching behavior. Furthermore, the interface-type switching normally does

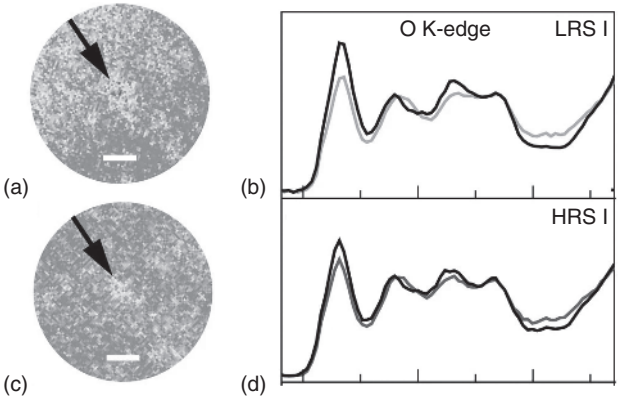

Figure 1.10 (a, c) XPEEM images of an $SrTiO_3$-based device in (a) LRS and (c) HRS, showing a localized filament with changes of the O concentration. Scale bars: 1 μm. (b, d) O K-edge spectra obtained from the filament region [light curve for LRS in panel (b) and dark gray for HRS in panel (d)] and the surrounding region (black curves). Source: Modified from Baeumer et al. [71].

not require a forming process and can easily obtain a multilevel storage because it changes the resistance value by a uniform interface effect. Overcoming the forming randomness of memristors, devices could achieve excellent reproducibility and cell-to-cell uniformity [74].

The interface-type resistive switching mechanism was first reported by Sawa in 2008 [4]. According to the article, the *I–V* curves of the Ti/PCMO, Au/Nb:STO, and SRO/Nb:STO interfaces show rectifying *I–V* behavior, thus revealing the presence of Schottky contacts. In addition to the rectification, *I–V* curves for these interfaces exhibit hysteretic behavior indicative of resistive switching. Furthermore, they found the migration of $V_O^{\cdot\cdot}$ at the interface plays a key role in the resistive switching. Up to now, different devices with interface-type switching have been explored, including Pt/WO_{3-x}/Pt [75], Pt/ZnO nanorod/FTO [76], Pt/Nb:STO/Al [77], ZrO_2:Y/PCMO [78], InGaZnO (IGZO)/a-IGZO[79], and so on.

The resistive switching process in the interface-type switching is schematically illustrated in Figure 1.11, using n-type semiconductor as an example [74, 80]. n-Type semiconductor forms a Schottky barrier when in contact with a metal with a large work function (such as Pt or SRO) and forms an Ohmic contact when associated with a low work function metal (such as Ti). In the conventional Schottky model, the capacitance is given by $C = \frac{\varepsilon_0 \varepsilon_S S}{W_d}$, where W_d is the width of the depletion layer, ε_0 is the relative dielectric constant of a vacuum, ε_s is the semiconductor relative dielectric constant, and S is the cell area. This equation indicates that LRS is achieved by tunneling through the Schottky barrier with a narrow W_d, while HRS is created by inhibited tunneling at the Schottky barrier with a wide W_d. With the application of a negative bias (Figure 1.11a), positively charged oxygen vacancies are attracted to the electrode narrowing the barrier, and the device switches to the LRS. A positive bias will result in the repulsion of the oxygen vacancies and in the restoration of the barrier width, and the device switches back to HRS (Figure 1.11b).

The current lack of full understanding of the underlying switching mechanisms remains a major challenge for interface-type memristive devices and a significant obstacle to their widespread applications. For this reason, in the past few years, a variety of materials characterization techniques have been employed to clarify the switching mechanisms in interface-type memristive devices, including the combination of TEM and electron energy-loss spectra (EELS) [81], spectromicroscopy studies [82], and so on.

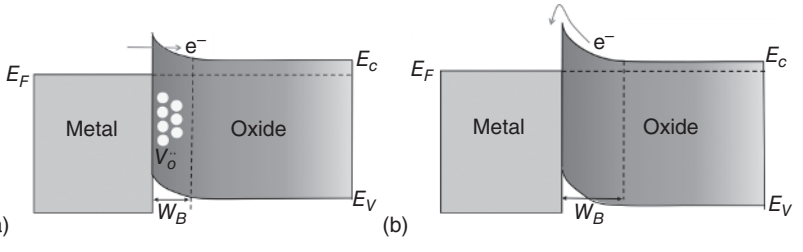

Figure 1.11 The interface-type resistive switching mechanism for a representative n-type semiconductor. (a) In the LRS, $V_O^{\cdot\cdot}$ accumulate at the interface, reducing the depletion width. (b) In the HRS, there are less $V_O^{\cdot\cdot}$ at the interface, increasing the depletion width.

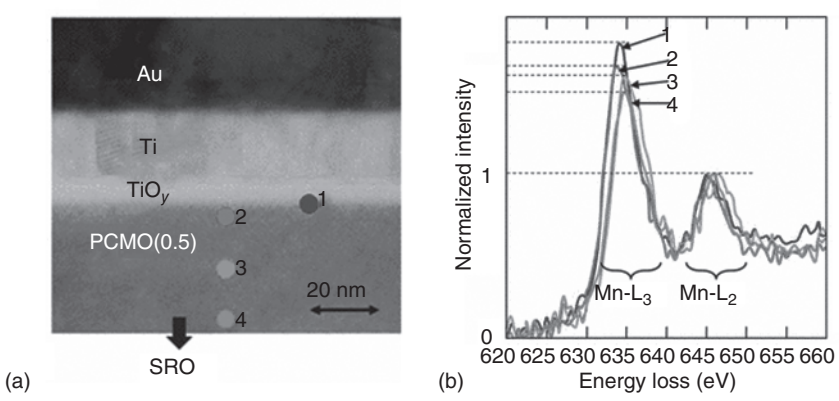

Figure 1.12 (a) Cross-sectional TEM image of Ti/PCMO junction. (b) Electron energy-loss spectra of Mn L-edge at several positions in Ti/PCMO junction indicated in (a). Source: (b) Asanuma et al. [81]. Copyright 2009, American Physical Society.

Combination of TEM and EELS As an example, the migration of $V_{\ddot{O}}$ in the Ti/PCMO interface was demonstrated by the combination of cross-sectional TEM and the EELS spectra, as shown in Figure 1.12. An amorphous TiO_y layer between the Ti electrode and the PCMO layer was clearly observed in the cross-sectional TEM (Figure 1.12a). Furthermore, the EELS of the Mn L-edge obtained at different positions in the PCMO layer was carried out to confirm the diffusion of oxygen ions at the interface. As seen in Figure 1.12b, the peak intensity ratio of Mn-L_3 and Mn-L_2, I(L_3)/I(L_2), decreased with increasing distance from the boundary between the TiO_y and the PCMO layers, indicating the valence of the Mn ion in the vicinity of the interface was smaller than that far from the interface. The above results suggest that the number of oxygen vacancies in the vicinity of the interface was increased due to the migration of oxygen ions from the PCMO layer to the Ti electrode.

Spectromicroscopy Studies Figure 1.13 shows spectromicroscopy results using the absorption current and photoemission electrons of the Au/Al/PCMO/CMO/PCMO/Pt device in the LRS and HRS, respectively. There are three different regions in Figure 1.13a, b: Au/Al/PCMO, Au/PCMO, and PCMO. Au/PCMO and PCMO, respectively, are the most (light) and least (dark gray) conductive in both resistive states. A significant change in current occurred in the Au/Al/PCMO region, with high (light gray) and low (dark gray) current intensity in the LRS and HRS, respectively, indicating the Al top electrode plays a key role in the resistive switching. Furthermore, from Al 2p photoelectron peaks and spectromicroscopy spectra (Figure 1.13d–f), one can clearly observe the oxidized state of Al in the Au/Al/PCMO region changes a lot when the device switches from HRS to LRS. This indicates that interfacial oxidation of the Al electrode in Al/PCMO acts as a reservoir of oxygen during the resistive switching.

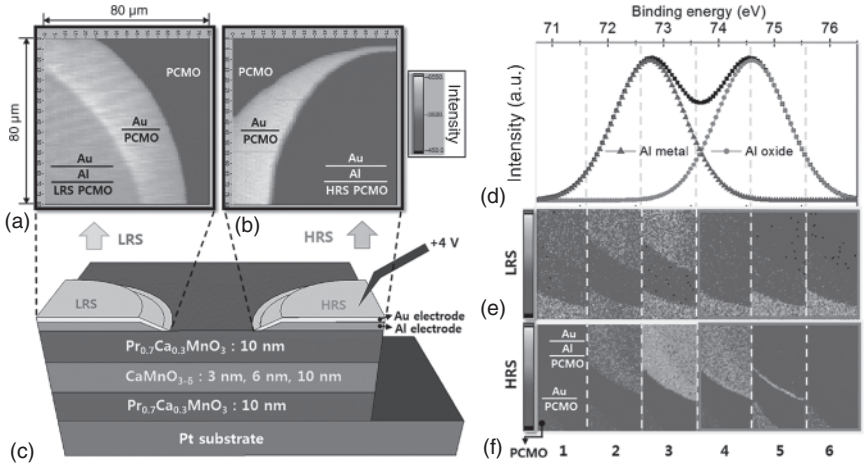

Figure 1.13 Spectromicroscopy results using the absorption current and photoemission electrons. Contrast images of absorbed electron intensity from the electrode areas of (a) LRS and (b) HRS. (c) The schematic diagram of the Au/Al/PCMO/CMO/PCMO/Pt (substrate) device. (d) Typical Al 2p photoelectron peaks of metallic (dark gray) and oxidized (light gray) states of aluminum as a function of binding energy. The *x*-axis energy intervals correspond to the window of integration for the corresponding lower panel of (e) and (f). (e) and (f) The panels show a color plot of the spatial distribution of the intensity of photoelectrons with energies within the respective energy interval [as indicated by the energy scale of (d)]. The six panels in (e) correspond to the images of an electrode in the LRS, and the panels in (f) to the respective images of an electrode in the HRS. The upper and lower panels 1–3 indicate the increasing (gray) intensity of the Al metal electrode. Panels 4–6 indicate the intensity of the Al oxide signal. Clearly, the signal is very weak in the upper panels corresponding to the LRS. In contrast, the lower panels clearly indicate oxidation of Al in the HRS. In particular, panel 5 of (f) shows a strong and thin signal coming from the rim of the Al electrode. Source: Lee et al. [82].

1.3 Memristive Bioinspired Devices

The human brain is far superior to the digital computer in cognitive and classification tasks, especially in solving probabilistic and unstructured problems requiring low power dissipation. This is because the architecture of the human brain is completely different from that of the digital computer [83, 84]. In a standard digital computer, the data memory and processor are physically separated by a channel, and constant data movement is required while working. In the human brain, huge and complex neural networks composed of gigantic amounts of neurons massively interconnected by an even larger number of synapses are responsible for computing and memory. Unlike a digital computer, information storage and processing happen at the same time in the brain [85].

Taking inspiration from the architecture and principle of the human brain, neuromorphic computing that aims to construct energy efficient and fault tolerant computing systems may have great potential in the future artificial intelligence (AI), big

data, Internet of things (IoT), etc. [86]. In particular, devices that can reproduce the functionalities of biological synapses and neurons are building blocks in the construction of such neuromorphic systems. Fortunately, the emergence of memristive devices, with inherent dynamics resembling biological synapses and neurons, provides a feasible way to construct neuromorphic computing systems [87, 88]. For instance, one compact memristive device is enough to reproduce some functions of a biological synapse. Moreover, the vector–matrix multiplication, which is believed to be the most data-intensive work in neural networks, can be naturally performed in a cross-bar array of memristive devices on the physical level based on Ohm and Kirchhoff laws. These features endow memristive devices ideally suitable for implementing highly efficient neuromorphic computing systems.

1.3.1 Memristive Synapses

It has been found that the human brain is composed of $\sim 10^{11}$ neurons and $\sim 10^{15}$ synapses. All human perception, emotion, learning, forgetting, and memory are performed by this complex neural network with building blocks of neurons and synapses. A neuron works to generate and transmit action potentials in the neural networks. A synapse is a specialized junction where two neurons contact and communicate with each other, as shown in Figure 1.14a, and plays a crucial role in the process and storage of information. The presynaptic side of the synapse is an axon terminal of the presynaptic neuron, while the postsynaptic side is the dendrites. An action potential, or nerve impulse, arrives at the axon terminal and triggers the presynaptic neuron to release neurotransmitters; these neurotransmitters bind to the receptors on the postsynaptic membrane and causes a transient postsynaptic membrane depolarization and then generate the excitatory or inhibitory postsynaptic potential (EPSP or IPSP), depending on the transmitting efficiency of the synapse. This transmitting efficiency of a synapse is not fixed but can vary as a result of the activities of pre- and postsynaptic neurons, which is termed as synaptic plasticity. In other words, the synaptic weight, that is, contact strength, is flexible and can be modified according to the activities of the relative neurons [90].

In biological system, synaptic plasticity performs different time courses ranging from milliseconds to hours, days, and even the whole lifetime. Therefore, with regard to the time course of the plasticity, synaptic plasticity can be roughly divided into short-term plasticity (STP) and long-term plasticity (LTP), as shown in Figure 1.14b [91]. It is found that STP allows the synapses to perform critical functions, such as fast response and information filtering. Furthermore, the synaptic plasticity exhibits the activity-dependent characteristic; weak tetanic induces only STP, whereas strong trains of stimulus induce LTP. Different from STP, LTP is thought to be crucial during synaptic development and for regulating neural circuits in the adult brain.

Given that one nanoscale memristive device can replicate diverse synaptic functions, it shares a similar structure and working principle to the biological synapse. These enable the memristive device to be a promising candidate as synaptic element to build neuromorphic computing systems. To date, encouraging progress has been achieved in the implementation of both STP and LTP using

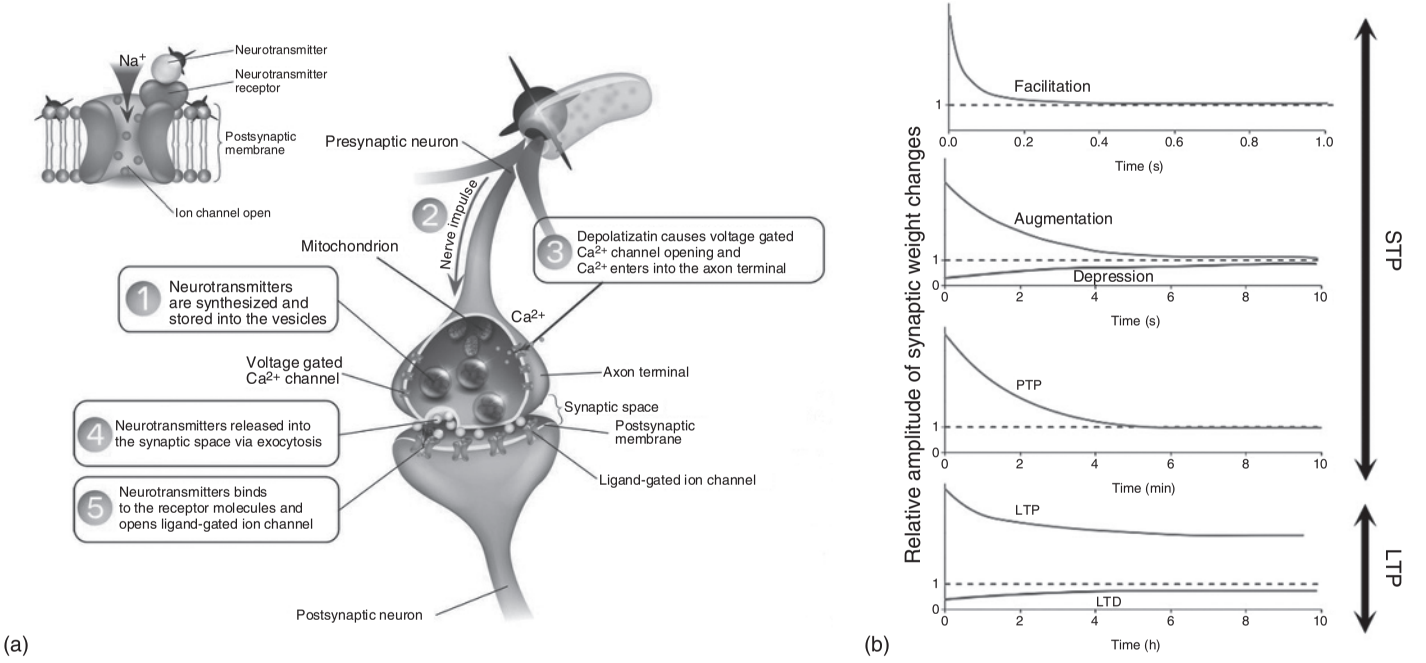

Figure 1.14 Biological synapses and its plasticity. (a) A biological synapse is formed at the axon terminal with the dendrites of other neurons. When a nerve impulse arrives in the presynaptic axon terminal, neurotransmitter molecules are released from synaptic vesicles into the synaptic cleft. Neurotransmitters are then bound to specific receptor proteins, causing the generation of electrical or chemical signals in the postsynaptic cell. Source: John et al. [89]. (b) Different forms of activity-induced synaptic plasticity in biological synapses: synaptic facilitation/depression, augmentation, post-tetanic potentiation (PTP), and long-term potentiation/depression. The first three are the short-term plasticity (STP), and the last one is the long-term plasticity (LTP). Source: Nicholls et al. [94].

memristive devices. Therefore, below we discuss short-term memristive synapses and long-term memristive synapses reported recently.

1.3.1.1 Short-Term Memristive Synapses

Numerous forms of synaptic plasticity lasting on the order of milliseconds to several minutes have been termed as STP, including synaptic facilitation/depression, augmentation, and post-tetanic potentiation (PTP), as shown in Figure 1.14b [91]. Synaptic facilitation (or depression) occurs when a brief train of stimuli is applied to a presynaptic nerve, in which the amplitude of EPSP progressively increases (decreases). In contrast, PTP happens when a relatively long high-frequency train of stimuli is applied to the presynaptic neuron and an intermediate phase between synaptic facilitation and PTP is an augmentation, which is introduced by stimulus trains with moderate duration. Although facilitation, PTP, and augmentation are all referred to as STP, they spin different temporal domains. Facilitation decays about a few hundred milliseconds, whereas the decay of augmentation and depression lasts over a period of several seconds. PTP can persist for tens of minutes. It is found that these STP play important roles in short-term adaptations to sensory inputs and short-term memory and are helpful in filtering out some unnecessary information.

In biological systems, paired-pulse facilitation (PPF) and paired-pulse depression (PPD) are the most important learning rules of STP and play a key role in decoding the temporal information for auditory or visual signals. In PPF, synaptic current evoked by the second spike is increased when the second spike closely follows a previous spike, as shown in Figure 1.15a [92, 94]. Furthermore, the magnitude of the enhancement is determined by the time interval between the two spikes, and a smaller interval gives rise to a larger synaptic current enhancement. In contrast, PPD describes the opposite phenomena, where the synaptic current evoked by the second spike is decreased when the second spike closely follows a previous spike [93], and the magnitude of the decrease is determined by the interval between the two spikes, which is similar to PPF (Figure 1.15b). It is found that PPF (PPD) is highly related to an increased (decreased) residue in presynaptic Ca^{2+} concentration left over from the first stimulus, which results in an increase (decrease) in the number of neurotransmitters released at the synapse when the second stimulus is applied [95].

As the most important STP, PPF has been implemented in many memristive devices with volatile resistive switching behavior [96–99]. Zhu et al. demonstrated PPF in the three-terminal in-plane lateral memristive devices [96], as shown in Figure 1.16. The indium–zinc–oxide (IZO) channel was self-assembled on phosphorus (P)-doped nanogranular SiO_2 proton conductive films at room temperature. The channel conductance can be modulated in a volatile way due to the proton-related electrical double-layer effect. In this device, the presynaptic spikes are applied on the in-plane gate, and the conductance of the channel is regarded as the postsynaptic response, that is, excitatory postsynaptic current (EPSC) or inhibited postsynaptic current (IPSC) (see Figure 1.16b). Figure 1.16c shows the EPSC evolution over time by applying two consecutive presynaptic spikes on the in-plane gate. It is clearly observed that the peak value (A2) of the EPSC triggered

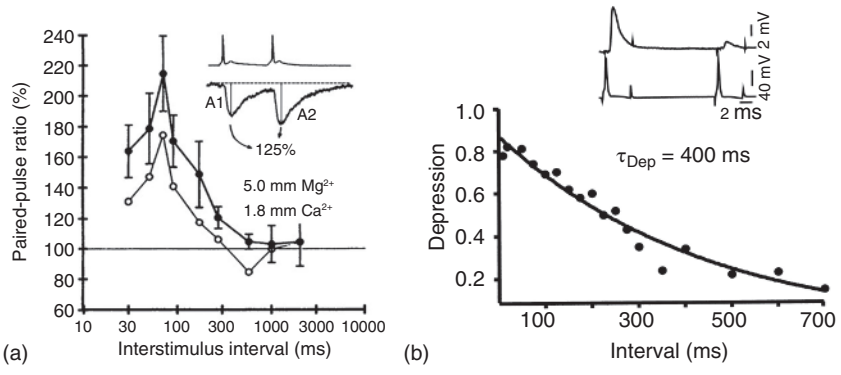

Figure 1.15 Short-term synaptic plasticity. (a) Paired-pulse facilitation (PPF). Source: Debanne et al. [92]. (b) Paired-pulse depression (PPD). Source: Waldeck et al. [93].

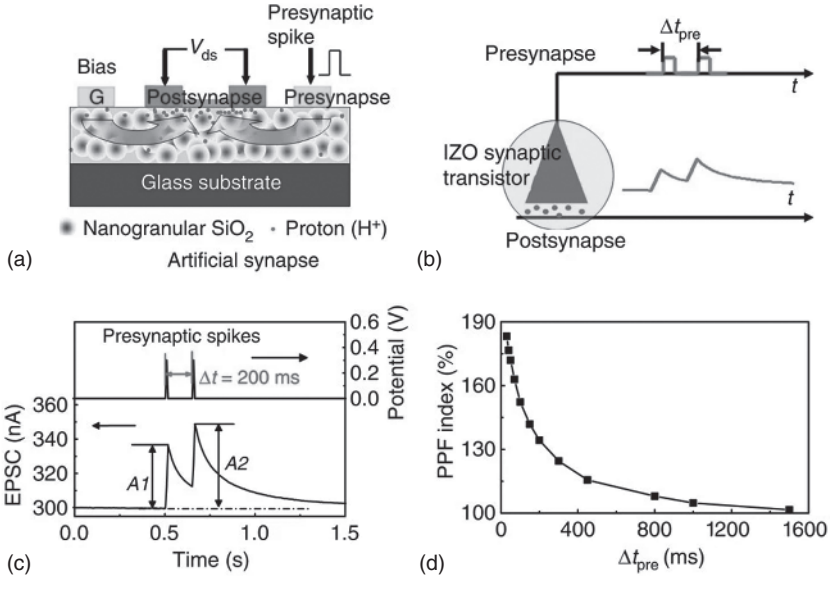

Figure 1.16 PPF implementation in the three terminal in-plane lateral memristive device. (a) Schematic diagram of the device structure. (b) Schematic image of the implementation approaches. (c) A pair of presynaptic spikes applied and the experimental response of the device. *A*1 and *A*2 represent the amplitudes of the first and second EPSCs, respectively. (d) PPF index, defined as the ratio of *A*2/*A*1, plotted as a function of interspike interval Δt_{pre}. Source: Zhu et al. [96].

by the second presynaptic spike is larger than that by the first presynaptic spike (A1). The PPF index, defined as the ratio of A2/A1, gradually decreases with the increase of the interspike interval, as shown in Figure 1.16d. That is because the transient accumulation of protons after the first spike will gradually fade as the interspike interval increases. The dependences of the PPF index on the interval follow a double exponential function in biological synapses and some memristive emulators.

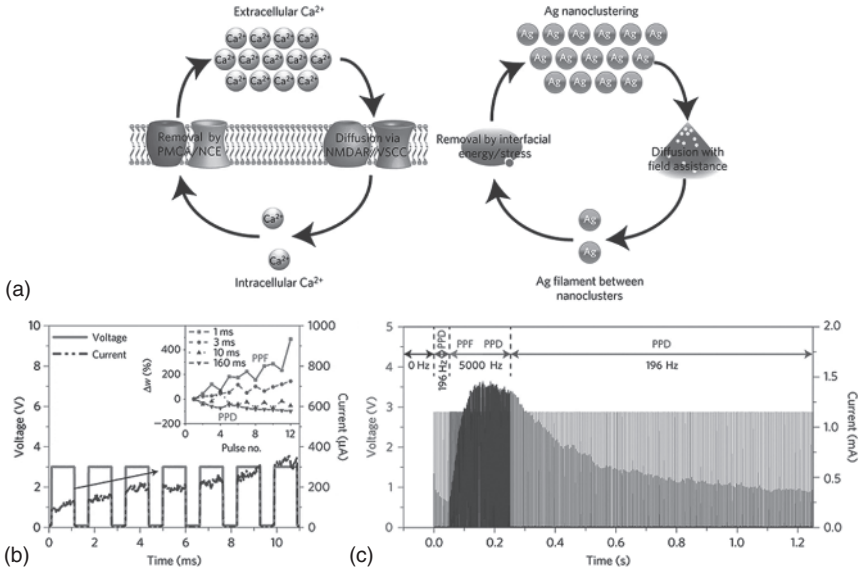

Figure 1.17 Biorealistic memristive synapses realized in diffusive memristive devices. (a) Schematic illustration of the analogy between Ca^{2+} and Ag dynamics in the diffusive SiO_xN_y:Ag memristive device. (b) Experimental demonstration of short-term synaptic PPF and PPD behavior by applying multiple subsequent voltage pulses (3 V, 1 ms) with different time intervals between 1 and 160 ms. (c) Experimental demonstration of PPD following PPF in the diffusive SiO_xN_y:Ag memristive device. The inflection effect from PPF to PPD under stimuli with the same frequency (5000 Hz) is a result of the gradual depletion of silver at one electrode and accumulation at the other. Source: Wang et al. [52].

Recently, Wang et al. first realized both PPF and PPD in two-terminal diffusive memristive devices with threshold switching behavior based on Ag-doped SiO_xN_y [52], as displayed in Figure 1.17. In their device, threshold switching is related to the formation of Ag filament through Ag cluster migration driven by electric field, and then the filament spontaneously ruptures driven by minimization of the interfacial energy between Ag and the dielectric after removing the external electric field. It is proposed that this kind of diffusive memristive devices performs significant similarities to the biological synapse in terms of ion diffusive dynamics, dynamic balance, and regulating roles, as schematically shown in Figure 1.17a. The experimental demonstration of PPF and PPD is shown in Figure 1.17b,c. High-frequency pulses (short t_{zero}) trigger facilitation (PPF), while low-frequency pulses trigger depression (PPD). More interestingly, the inflection from facilitation to depression in biological synapses, an effect solely induced by an increased number of stimulation pulses at the same frequency, that is, PPD following PPF induced by a series stimuli with same frequency, can also been biologically mimicked (see the current evolution under stimuli with 5000 Hz shown in Figure 1.17c). This inflection effect from PPF to PPD under stimuli with the same frequency is attributed to the gradual depletion of silver at one electrode and accumulation at the other. Similar PPD following PPF phenomena have been recently demonstrated in a biomolecular memristive device by Najem and his coworkers [100].

As mentioned before, there are several forms of STP with different time courses, including facilitation (tens of milliseconds), synaptic augmentation (seconds), and PTP (tens of seconds to minutes). It means that STP in biological synapses spans broad timescales from milliseconds to minutes. However, the most reported STP behaviors in memristive devices only exhibit certain specific timescales limited by their intrinsic micro-physicochemical processes during resistive switching. Recently, Zhang et al. emulated dynamic synaptic plasticity over broad timescales from milliseconds to days in the Ag/MgO/Pt ECM device [101]. Their Ag/MgO/Pt device exhibits volatile switching behavior, and its data retention of LRS can be tuned from millisecond to several 10 seconds through controlling the amplitude of applied external pulses. Therefore, many forms of STP have been mimicked including facilitation, augmentation, and PTP. It is proposed that the switching dynamics is attributed to the formation and spontaneous rupture of silver nanofilaments. By adjusting the thickness of filaments via applying the stimulus with different amplitudes, different timescales of STP can be realized. In addition to tuning external programming stimulus, mediating STP can also be achieved by controlling the orientation of silica mesopores in the device of Ag/Ag_2S/silica mesopore/ITO. [98]. The dielectric silica layer with vertical mesopores can facilitate the rupture of a conductive pathway, which results in short relaxation time for LRS (0.5 seconds) compared with parallel mesopores (3 seconds) and dense amorphous silica (>10 seconds). Thus, the time constants of PPF emulated in these devices present different timescales.

1.3.1.2 Long-Term Memristive Synapses

Unlike STP, LTP including long-term potentiation (LTPot) and long-term depression (LTD) refers to synaptic plasticity that lasts for hours or even days. LTPot was first observed in the hippocampus, where high-frequency repetitive activation of excitatory synapses caused a potentiation of synaptic connection that could last for hours or even days. Note that LTPot lasts longer than STP, but it still decays over time, as shown in Figure 1.18a. Moreover, the decay rate of LTPot depends on the duration and intensity of the stimulus [102, 104]. Figure 1.18a shows the LTPot response of the CA1 pyramidal neurons to three different stimulus conditions. The LTPot triggered by a single 100 Hz stimulus train decays back to zero over the next two hours; the potentiation decays less rapidly after four stimulus trains and becomes much slower after eight stimuli trains – with 80% of the potentiation persisting after two hours. Similar to LTPot, LTD also performs different time course of decay depending on the stimulus conditions. Both LTPot and LTD involve an increase in postsynaptic calcium concentration. A relatively large increase results in LTPot; a smaller increase leads to LTD [105]. Recently, LTP has garnered many interests because it provides an important key to understanding some of the cellular and molecular mechanisms of memory formation.

For LTP, the synaptic plasticity is dependent on the activities of pre- and postsynaptic neurons according to STDP [103] or Bienenstock–Cooper–Munro (BCM) learning rule [90, 106, 107]. The classical pair-STDP rule is a temporally specific extension of the Hebbian associative plasticity, which describes the synaptic weight depending on

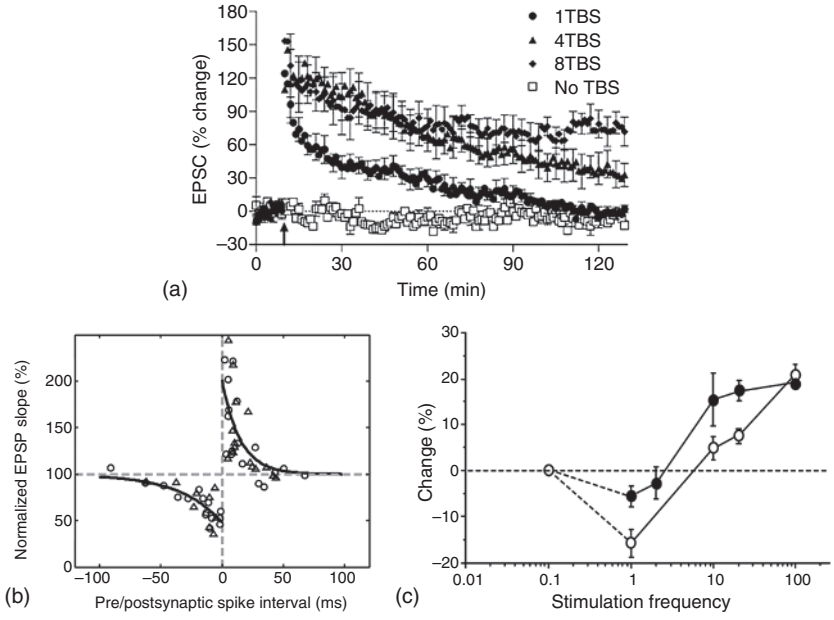

Figure 1.18 LTP in biology. (a) Long-term potentiation (LTPot) response of the CA1 pyramidal neurons to three different stimulus conditions. Source: Raymond and Redman [102]. (b) Spiking time-dependent plasticity (STDP). Source: Froemke and Dan [103]. (c) Bienenstock–Cooper–Munro (BCM) learning rule. Source: Kirkwood et al. [90].

the interval between pre- and postsynaptic spikes, as shown in Figure 1.18b. Specifically, if a presynaptic spike precedes a postsynaptic spike with a short interval, the synaptic weight enhances, whereas the synaptic weight decreases if the postsynaptic spike precedes a presynaptic spike. Moreover, there is no change of synaptic weight if the time interval between pre- and post-spike is too large. Actually, the abovementioned pair-STDP is Hebbian STDP. There are other three types of STDP, including the anti-Hebbian STDP, the symmetrical STDP, and the visual STDP learning rule observed in different types of synapses [108, 109].

In addition to STDP, BCM learning rule is another fundamental activity-dependent learning rules. According to BCM learning rule[107], the synaptic weight modulation performs frequency-dependent and sliding threshold characteristics, as schematically shown in Figure 1.18c [90]. In particular, high-frequency stimulation leads to potentiation, and low-frequency stimulation leads to depression. Furthermore, there exists a threshold frequency at which the synaptic weight can be maintained. More importantly, this threshold frequency is not fixed, and it will shift according to the priming neuron activity. For example, after a period of excited synaptic activity, the threshold will slide to a higher frequency, which can effectively prevent serious excitotoxicity stimulation. Similarly, the threshold will slide to lower frequency after a period of decreased activity, which is helpful for improving the synaptic modulation efficiency.

In this part, we will focus on the implementation of STDP and BCM learning rules in the memristive devices. It is well known that STDP is one of the most important LTP and the prevalent weight updating rules used in the spiking neuron networks [110]. There are two approaches to realize STDP. One is phenomenological implementation through overlapping the manually and carefully designed programming pulses to encode the spike timing information in the amplitude or duration of the effective applied pulses on the devices. The other one is biorealistic implementation through non-overlapping programming pulses using second-order memristive devices or combining a volatile memristive device with a nonvolatile memristive device. In addition, BCM learning rule describes the frequency-dependent synaptic plasticity with sliding threshold characteristics. However, previously demonstrated BCM rules in memristive devices mostly perform frequency-dependent characteristics without a sliding threshold feature, which is actually spike-rate-dependent plasticity (SRDP). Similar to STDP, biorealistic implementation of BCM rules requires second-order memristive devices with internal short-term dynamics.

Recently, phenomenological implementation of STDP learning rules has been intensively demonstrated using memristive devices in different material systems [79, 111–115]. However, this kind of STDP implementation is not biorealistic since the presynaptic and postsynaptic spikes pose the same profile and STDP is achieved via simple overlapping spikes. In fact, synaptic plasticity in biology is in turn modulated by other secondary state variables such as the postsynaptic calcium ion (Ca^+) concentration, rather than directly by the spikes. It is found that the postsynaptic Ca^+ concentration rises right after the excitation stimulus and then spontaneously decays over time after stimuli, which provides an internal timing mechanism to encode the relative timing information of the spikes [116]. Lu and his coworkers developed second-order memristive devices to biorealistically implement STDP learning rules through non-overlapping approach [30, 117]. In the so-called second-order memristive devices, there are two state variables. The one with long-term dynamics directly determines the device conductance, while the second one with short-term dynamics has an impact on the conductance by affecting the first state variable. This second state variable plays a role similar to postsynaptic Ca^+ concentration in regulating synaptic plasticity; therefore, biorealistic implementation of STDP without the need of pre/postsynaptic pulses overlapping can be achieved in second-order memristive devices. The local temperature [117] or the mobility of oxygen vacancies [30] can be treated as the second state variables, since they perform short-term dynamics in memristive devices.

Furthermore, STDP rule is implemented in the second-order memristive device of Pd/Ta_2O_{5-x}/TaO_y/Pd [117]. In this device, the size of the conduction filaments is the first state variable with long-term dynamics, while the local temperature of the device is the second-state variable with short-term dynamics. There are two parts in the pre- and postsynaptic spikes: a programming element with high-voltage short duration and a heating element with low-voltage long duration. The device local temperature elevates, but conductance does not change upon applying the heating element alone. Then, the local temperature spontaneously decays after removing the pulses, but this elevated local temperature facilitates the filament growth during

the programming element. When the presynaptic spike arrives earlier than the postsynaptic spike (i.e. in the case of $\Delta t > 0$), the postsynaptic spike will be affected by the temporal heating effect from the heating element in the presynaptic spike. The smaller Δt induces the much higher local temperature; as a result, much bigger size of filament is obtained in the device. The sign of conductance change is dominated by the final spike applied on the device, whereas the size of the conductance change relies on the pre/postsynaptic spike interval. In the opposite case ($\Delta t < 0$), the conductance decrease can be obtained by similar arguments. This local temperature plays a role similar to postsynaptic Ca^+ concentration in encoding the timing information of pre/postsynaptic spikes. It should be noted that the obtained conductance change in STDP rules stems from the modulation of the first state variable (i.e. the size of conduction filaments) and thus is long term, even though the timing information is encoded in the local temperature with short-term dynamics. The nonvolatile memristive devices without short-term dynamics can also be adopted in biorealistic STDP implementation by combining with a volatile element in series [52].

Biorealistic implementation of BCM learning rules with sliding threshold frequency also requires second-order memristive devices, since the sliding threshold frequency calls for variables with short-term dynamics. Lu and his coworkers demonstrated BCM rules in the Pd/WO_x/W second-order memristive devices [30]. The current of LRS state spontaneously decays after the removal of the external electric field, as shown in Figure 1.19a–c. The current decay process is also known as forgetting effect, retention loss, or memory loss characteristics. Taking advantage of this forgetting effect, one can realize biorealistical implementation of BCM learning rule with a sliding threshold frequency. The conductance of the device at any given instant depends not only on the stimulus but also on the state of the device, which is related to the forgetting process. As given in Figure 1.19b, the same stimulus (10 Hz) can trigger either current decrease (in step 2, following 200 Hz stimulus) or current increase (in step 4, following 1 Hz stimulus) depending on the previous activity. Thus, the modulation efficiency of a stimulus with a given frequency is highly related to the previous stimulus frequency, which is in line with the sliding threshold frequency in biological BCM rules. The realized BCM rules are given in Figure 1.19c. The detailed measurement approach is given as follows: First, one of three previous activities (ten pulses at either 10, 20, or 50 Hz) are applied on the device with the same state. Second, a stimulus with different frequency (the abscissa) is applied on the device, and the resultant net current change (the ordinate) is recorded. It is clearly shown that high-frequency stimulation leads to the potentiation and low-frequency stimulation leads to the depression. Furthermore, the threshold frequency slides as a function of the previous stimulus. This result is in good agreement with the biological BCM rules. This biorealistic BCM learning rule has also been demonstrated in cone-shaped ZnO memristive device with forgetting effect [119]. Very recently, Xiong et al. [118] realized the tunable forgetting rate by engineering the electrode/oxide interface by controlling the electrode composition in STO memristive devices, as shown in Figure 1.19d,e. The BCM rules with tunable sliding frequency thresholds are biorealistically demonstrated (see Figure 1.19f).

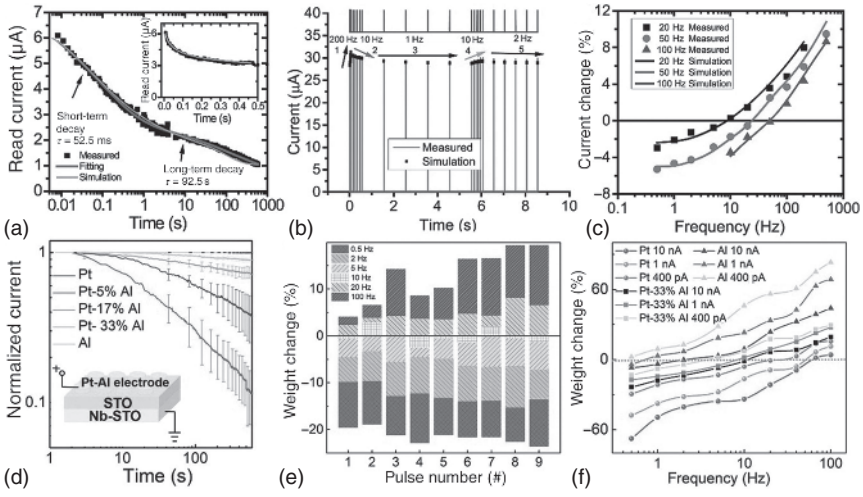

Figure 1.19 Biorealistic BCM learning rules obtained in second-order memristive devices. (a) Memristive device forgetting effect observed in the device of Pd/WO_x/W. (b) The memristive device response to consecutive programming pulse trains (1 V, 1 ms) at different frequencies. The same stimulus (10 Hz) can trigger either current decrease (in step 2, following 200 Hz stimulus) or current increase (in step 4, following 1 Hz stimulus) depending on the previous activity. (c) The experimental BCM rules obtained by controlling the priming stimuli frequency. Source: (a–c) Du et al. [30]. (d) Tunable forgetting effect observed in $SrTiO_3$ (STO) memristive device with different electrodes (Pt, Pt-5% Al, Pt-17% Al, Pt-33% Al, Al). (e) The current change of the Pt-33% Al/STO/Nb-STO device by applying nine pulses (1 V, 10 μs) with different frequencies. (f) Frequency threshold of the BCM rules can be tunable through modulating the Al content in the electrodes (0%, 33%, 100%) or controlling the device states (400 pA, 1 nA, 10 nA). The frequency threshold shifts to low frequencies when the Al content in the electrodes is higher and the conductance level is lower. Source: (d–f) Xiong et al. [118].

1.3.2 Memristive Neurons

Besides synapses, another fundamental element in biological neural networks is neuron. A biological neuron consists of several parts: the soma, the dendrites, the axon, and the neuronal membrane [120], as schematically shown in Figure 1.20a. The information encoding function of neurons is mainly realized by the change in their membrane potential. The resting equilibrium membrane potential is determined by the concentration gradients of ions across the membrane. The ion channels on the membrane are much more permeable to K^+ than to Na^+, so the equilibrium potential of K^+ is about −70 mV when the neuron is at rest. The action potential is generated by the flow of ions through voltage-gated channels, as shown in Figure 1.20b,c. That is, the depolarization of the membrane caused by external stimulations will change the configuration of the Na^+ channels, resulting in the higher permeability to Na^+. As a result, there will be Na^+ influx through voltage-gated Na^+ channels, which forms the rising edge of the action potential and reverses the polarity of the plasma membrane. The voltage-gated Na^+ channels will then be closed, and the K^+ channels are activated, hence leading to an outward flux

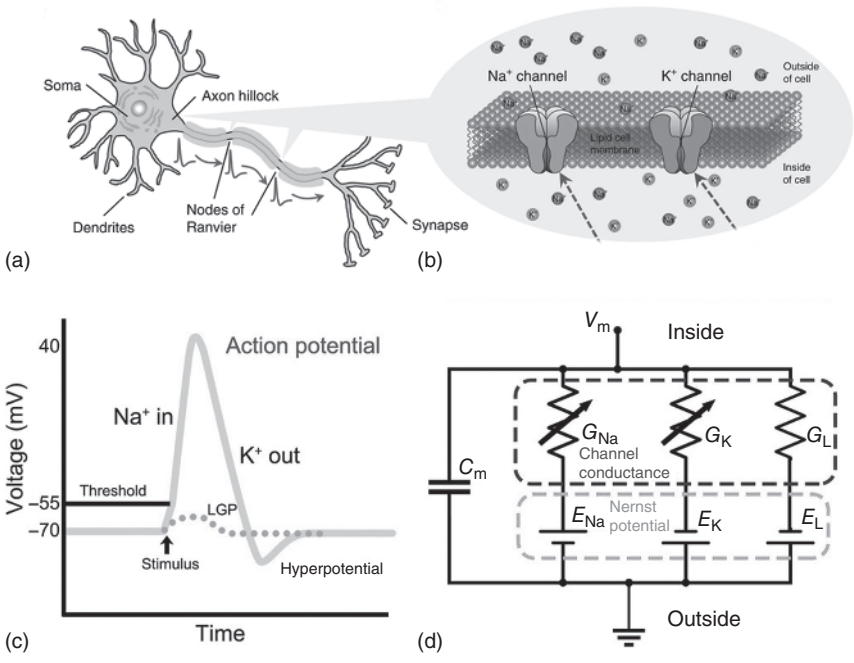

Figure 1.20 Biological neurons. (a) Schematic of a biological neuron, including soma, dendrites, axon, and nucleus. (b) Schematic of neuronal membrane. Source: (a, b) Yi et al. [120]. (c) Action potential in a biological neuron. (d) Hodgkin–Huxley neuron model. Source: (c, d) Yang et al. [47].

of K^+ ions. This forms the dropping edge of the action potential and returns the membrane potential to the resting state.

The above neuronal dynamics can be described by the integrate-and-fire (IF) model, leaky-integrate-and-fire (LIF) model, and Hodgkin–Huxley (HH) model [121]. IF and LIF models are mainly based on the insight that pulsatile spike is a threshold process. In the IF neuron model, the spikes of the presynaptic neuron, scaled by the strength of the corresponding synapses connecting with the dendrites, are applied to the neuron and then cause EPSCs or IPSCs due to the membrane depolarization. These EPSCs will be temporally and spatially integrated and induce the neuron membrane boost that is known as the local graded potential (LGP). An action potential is triggered when LGP reaches the threshold. If the LGP is below the threshold, IF neuron will retain that voltage boost continuously until it fires again. This characteristic is not in line with observed neuronal behavior. In fact, LGP shows short-term dynamics and results in a sub-threshold membrane boost that soon leaks out in a short time in biological neurons. Thus, a leaky term is added to the membrane potential to form an LIF neuron model. In an LIF neuron, the sub-threshold membrane boost will leak out in a period of time, which endows the neuron to implement time-dependent memory. The IF and LIF models give a bioplausible description of neural behavior but provide only a weak link to the

underlying biophysical causes of electrical activity, and these two models are rather limited in predicting the precise time course of voltage during and after a spike.

In contrast, the HH model is the detailed biophysical neuron model that describes the dynamics of ion channels on the neuron cell when it is spiking and widely accepted in computational neuroscience. A typical HH neuron model based on the parallel thought of a simple circuit is shown in Figure 1.20d. The HH model treats each component of a neuron as an electrical element. The neuron membrane is represented as a capacitance (C_m); the conductance of ion channels is presented by resistors with programmable resistance. The leak channels are presented by a linear resistor (G_L). Nernst potential generated by the difference in ion concentration is represented by a battery (E_{ions}). Compared with IF and LIF neurons, HH neuron is very complex because it is a nonlinear system and cannot be solved analytically, which limits its application in artificial neuron networks. However, the development of memristive devices opens a new avenue for hardware artificial neurons.

In biological systems, scalable neurons are indispensable building blocks, in addition to compact synapses, for constructing large-scale neuromorphic computing systems. Thus, the development of scalable artificial neurons is an active area of research in the past few years, and some stirring progress have been made with the emergence of memristive devices [122–124]. Note that the design of memristive neurons is much different from that of artificial synapses, since they play quite different roles in neural networks. Rich synaptic functions can be generally emulated in a single memristive device via its conductance changes representing synaptic weight modulation. In contrast, one memristive alone normally is not sufficient as a substitute of a neuron; a hybrid circuit consisting of CMOS transistors and memristive devices is mostly needed to emulate a neuron [125]. Here, the goal is to mention that the introduction of memristive devices significantly simplifies the neuron circuits compared with those based on CMOS transistors only.

As mentioned above, there are many neuron models including IF neuron, LIF neuron, HH neurons, and some extended and simplified versions of these models [121, 126, 127]. Actually, these neuron modes can be divided into two classes: bioplausible neurons consisting of IF and LIF neurons and biophysical neurons mainly referring to HH neurons [121]. IF and LIF neurons are focused on the threshold process generating a spike, while HH neurons are based on the biophysical dynamic details of ion channels in the neuron membrane. Bioplausible neurons are simple but prevalent in neuromorphic computing, while biophysical neurons describe some salient features of biological neurons that bioplausible ones fail to capture, such as hyperpolarization. It is found the hyperpolarization can prevent the spiking rate from going extremely high value, which is critical in the neuromorphic computing systems coding based on spike frequency and timing [128]. Some representative reports about bioplausible and biophysical neurons based on memristive devices are given in Table 1.1.

Table 1.1 Memristive neurons.

Memristive neuron	Auxiliary circuit	Device	Device size	Operation (voltage/current)	Switching type	Mechanism	References
Bioplausible neuron							
IF	Comparators	$Ge_2Sb_2Te_5$	Φ 20 nm	6 V/700 μA	Nonvolatile	PCM	[124]
LIF	Capacitor	Pt/SiO_xN_y:Ag/Pt	—	1.4 V/40 μA	Threshold	ECM	[129]
	Capacitor	$Ag/SiO_2/Pt$	$5 \times 5\ \mu m^2$	2 V/100 μA	Threshold	ECM	[130]
	MOSFET	Pt/SiO_x:Ag/Pt/$TaO_xTa_2O_5/Pt$	$10 \times 20\ \mu m^2$	2 V/300 μA	Pseudo-memcapacitor	ECM and VCM	[131]
	—	$GaTa_4Se_8$	$40\ \mu m^2$	40 V/20 mA	Threshold	MIT	[132]
	—	$Pt/FeO_x/Ag$	$2 \times 2\ \mu m^2$	4 V/10 mA	Threshold	ECM	[133]
Biophysical neuron							
HH	Voltage source and capacitor	$Pt/NbO_2/Pt$	$110 \times 110\ nm^2$	1.6 V/300 μA	Threshold	MIT	[123]
	—	$Pt/VO_2/Pt$	$50 \times 50\ nm^2$	1.2 V/3 mA	Threshold	MIT	[134]
	Comparator and resistor	W/WO_3/PEDOT:PSS/Pt	$50 \times 50\ \mu m^2$	2.7 V/1 μA	Bipolar/volatile	Proton inserting/extracting	[10]

IF neuron, the integrate-and-fire neuron; LIF, leaky-integrate-and-fire neuron; HH, Hodgkin–Huxley neuron; PCM, phase change memory cell; VCM, valence change mechanism; ECM, electrochemical metallization cell; MIT, metal–insulator transition.

1.3.2.1 Bioplausible Memristive Neurons

In 2016, Tuma et al. [124] successfully developed an IF neuron in a hybrid circuit consisting of a phase-change ($Ge_2Sb_2Te_5$, GST for short) device and an auxiliary circuit including comparators. The phase-change device is used to represent the membrane potential and realize the integration function with innate stochastic dynamics that arise directly from the physics of melt-quench-induced reconfiguration of the amorphous phases in GST. The fire function is realized by triggering a spike generator when LGP reaches the threshold values set by the comparator. Owing to the nonvolatile nature of resistive switching in GST, the leaky function is missed in this stochastic neuron. In 2018, Yang et al. [25] designed an LIF neuron in which an ideally volatile memristive device (Memristor 2) was adopted to represent membrane potential with short-term dynamics and thus realize leaky function. The circuit of this LIF neuron is shown in Figure 1.21. Memristor 1 presents nonvolatile resistive switching behavior with or without forgetting effect, which is used to represent the synapse receiving input spikes. These input signals scaled by the relative synaptic strengths then temporally and spatially integrate as V_{add} via the adder OP_1, which is the integration function of the neuron. Then, V_{add} is applied on Memristor 2 and evokes the resistance decrease of Memristor 2, which results in a boost of the divided voltage of RC (V_{out}). V_{out} plays a role like LGP does in biological neurons. A spike is

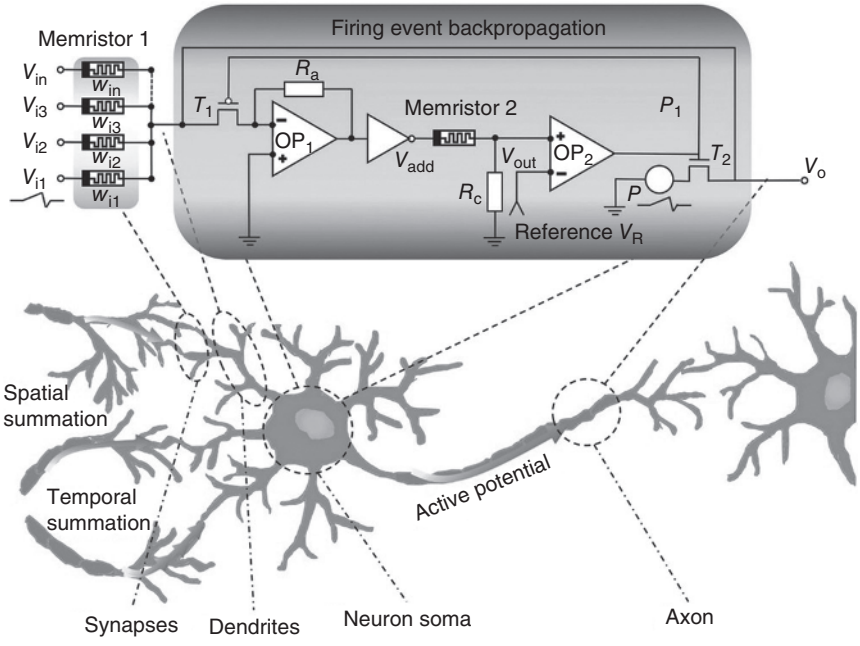

Figure 1.21 The LIF neuron implementation in the threshold-less memristive devices combined with comparators. In this LIF circuit, Memristor 1 represents the synapses to receive inputs from upstream neurons. Memristor 2 is a volatile second-order memristive device, which is used to mimic the dynamics of the local graded potential. Source: Yang et al. [25].

generated if V_{out} is larger than the reference value of comparator OP_2 (V_R), realizing the fire function. If V_{out} is lower than V_R, V_{out} will gradually leak out, owing to the volatile feature of Memristor 2, which is the leaky function of this neuron. Note that the resistive switching process in Memristor 2 is analog and without obvious threshold value. Thus, a comparator is required to realize the threshold spiking process. Furthermore, the spike generation is implemented with the help of a pulse generator (P), which makes it difficult for such neurons to achieve high-density integration.

In contrast, if the memristive device performs intrinsic threshold switching process, the LIF function of neurons can be realized using a much simpler auxiliary circuit without comparator and external pulse generator [135]. In this case, the threshold switching memristive device handles threshold spiking process. A capacitor is typically connected to the threshold switching memristive device in parallel to implement integration effect via the charging process. Wang et al. [129] recently developed an LIF neuron with a simple circuit composed of a diffusive memristive device and a capacitor in parallel, as shown in Figure 1.22a. In this LIF neuron, the capacitor acts as the membrane and realizes the leaky and integration effects of neurons, while the diffusive memristive device functions as the ion channel and implements the fire function. The output signal in this neuron is the current flow across the diffusive memristive device. To obtain a voltage spike, a resistor can be connected in series with a threshold switching device, as shown in Figure 1.22, and the output signal is represented by the divided voltage of this series resistor. When input pulses are applied on this LIF neuron, the capacitor charges with a time constant of R_sC and lifts up the voltage across the diffusive memristive device (CL loop in Figure 1.22b). The memristive device turns on by forming conducting filaments when the voltage reaches its threshold, and soon, the capacitor performs discharging through the memristive device (DL loop in Figure 1.22b) and induces the plunge of the voltage across the memristive device, resulting in it recovering to high resistance. Accompanied by this capacitor charging and discharging process, a voltage spike is generated. Zhang and his coworkers [130] developed this type of LIF neuron using an ECM cell of $Ag/SiO_2/Au$, and it was found that the spike frequency could be tuned by controlling the strength of input signals. In comparison with the abovementioned artificial neuron composed of comparators, this hybrid LIF

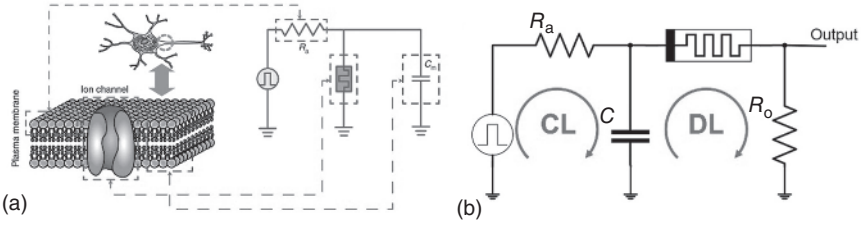

Figure 1.22 The implementation of an LIF neuron in the threshold memristive devices with parallel capacitors. (a) Schematic illustration of an artificial LIF neuron composed of a threshold memristive device and a parallel capacitor, in which the memristive device functions as the ion channel and the capacitor acts as the membrane. Source: Wang et al. [129]. (b) Schematic illustration of the LIF neuron circuit with voltage output.

neuron circuit is much simpler, since it typically comprises a threshold switching device and a capacitor in parallel. Thus, the reported artificial LIF neurons mostly belong to this type of LIF neurons so far. It is noteworthy that some LIF neurons with tunable integration time have been realized using memcapacitors [136, 137] or pseudo-memcapacitors (a diffusive memristive device with a series capacitor) [131] to replace normal capacitors.

Note that two-terminal memristive devices share similar structure with normal capacitors, that is, MIM sandwich structure. Thus, it is not surprising to find that some memristive devices work as capacitors at a given time, in particular at HRS state, and a capacitor is included in the equivalent circuits of some memristive devices. Therefore, it is not necessary to add a capacitor to implement the integration function of LIF neurons, at least for some memristive devices, meaning that an LIF neuron can be realized with a single component. In 2017, Pablo and his coworkers [132] reported a LIF neuron based on a single MIT memristive device, as shown in Figure 1.23. The sample shown in this figure is an MIT device based on $GaTa_4Se_8$

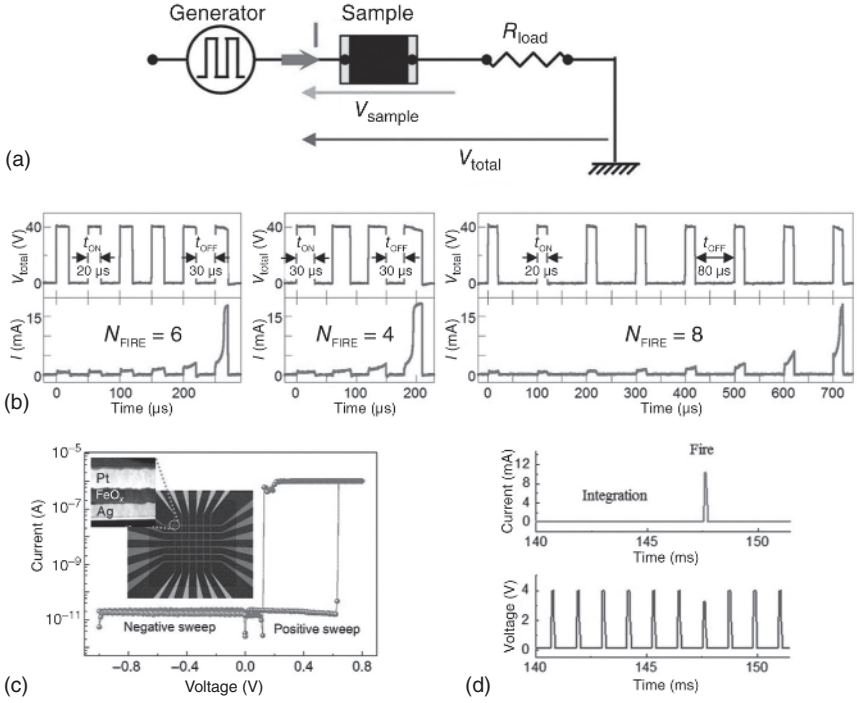

Figure 1.23 LIF neuron based on a single component of threshold memristive device. (a) Experimental setup in which the current flowing through the memristive device represents the output spike. (b) Experimental integrate-and-fire functionality realized in the single component of $GaTa_4Se_8$ MIT cell. Source: (a, b) Stoliar et al. [132]. (c) *I*–*V* characteristics of the Pt/FeO_x/Ag threshold memristive device. Inset: The cross-section view of the memristive device under high-resolution transmission electron microscopy (HRTEM) inspection. (d) The demonstration of integrate-and-fire behavior under continuous voltage pulse train based on the single Pt/FeO_x/Ag threshold memristive device. Source: (c, d) Zhang et al. [133].

with threshold switching behaviors. The current flowing through the MIT cell is the output signal. The working process of this LIF neuron is similar to those based on hybrid circuits with capacitors. Furthermore, the spiking frequency can also be tuned by controlling the input pulse parameters (see Figure 1.23b). In 2018, Zhang et al. [133] realized a highly compact LIF neuron with low power consumption using a single threshold switching device of Pt/FeO_x/Ag in a similar way, as shown in Figure 1.23c,d. Detailed experimental results indicate that the formation and automatic retrieval of silver filaments are the physical mechanism of threshold switching behavior. From the above discussions, we can conclude that threshold switching with volatile nature is very useful for implementing LIF neurons. Thus, this observed in many oxides has been exploited to realize bioplausible neurons with a compact structure [138]. In addition to memristive devices, some magnetic devices [139–141] were also exploited to realize some bioplausible functions of neurons, which is beyond the scope of this article.

1.3.2.2 Biophysical Memristive Neurons

Unlike bioplausible neurons that can be realized in a single memristive device, the biophysical neuron, that is, the HH neuron, involving complex dynamics of Na^+ and K^+ ion channels, requires much more complex circuits, and the progress on realization of artificial HH neurons is quite limited. In 2012, Pickett and his coworkers [123] developed an HH axon using two elements, each comprising an NbO_2 cell and a capacitor in parallel to function as sodium and potassium ion channels in the neuron membrane. These two elements are coupled with each other through a load resistor (R_{L2}), as shown in Figure 1.24a. The adopted NbO_2 memristive device performs threshold switching (see Figure 1.24b). The spike generated by this axon well resembles the biological spikes with hyperpolarization, as displayed in Figure 1.24c. The extended version with the stochastic effect of this HH axon is simulated by Saeed in 2017, [142]. Moreover, in 2018, Yi et al. [134] experimentally demonstrated the stochastic HH axon built with VO_2 MIT memristive devices in a similar circuit and realized most of the known neuron dynamics. Note that this circuit is typically termed as HH axon rather than HH neuron due to the fact that it mainly deals with the way of generating a spike highly resembling biological axons. Very recently, Huang and his coworkers [10] designed an artificial quasi-HH neuron with LIF functions based on a volatile memristive device with distinct nano-battery effect. The memristive device adopted here performs volatile analog switching behaviors, as shown in Figure 1.25. Unlike normal oxide memristive devices based on oxygen ion migration, the analog switching obtained in this device stems from proton migration with much higher mobility than oxygen ions. The protons come from the poly(3,4-ethylenedioxythiophene):polystyrene sulfonate (PEDOT:PSS) bottom electrode. The high ionic conductivity of protons fosters the enhancement of the battery effect in the device of W/WO_3/PEDOT:PSS. The hybrid neuron circuit is shown in Figure 1.25c. There are two memristive devices, M_1 and M_2, in the dedicated electrical circuit, in which M_1 acts as neuron membrane and realizes the LGP dynamics while M_2 functions as neuron axon and realizes firing an HH neuron-like spike. Since this memristive device has no threshold, the comparator is utilized to implement LIF functions in the first part of this circuit. If LGP reaches the reference

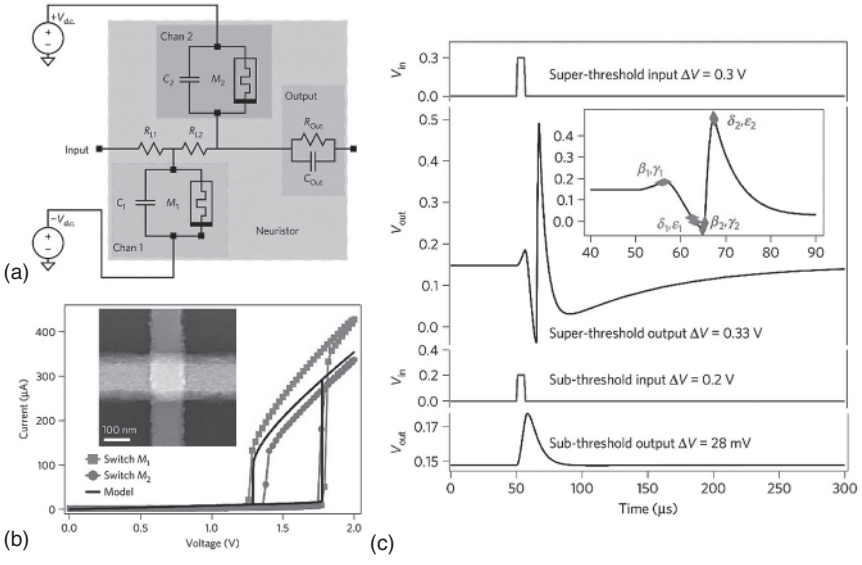

Figure 1.24 Memristive HH axon. (a) Circuit diagram of the HH axon. The channels consisting of Mott memristive devices (M_1 and M_2), each with a characteristic parallel capacitance (C_1 and C_2) and coupled through a load resistor of R_{L2}. (b) Threshold switching observed in the Mott NbO_2 memristive devices. (c) Simulated super-threshold 0.3 V input pulse and its corresponding spike output highly resembling the biological spikes. Source: Pickett et al. [123].

value of comparator, a falling edge is generated by the comparator and then triggers timer to generate a pulse with fixed width. This pulse carrying the timing information of input signals is applied on a simple circuit consisting of M_2 and a resistor R3 in series. The output spike is the divided voltage on R3, which highly resembles the neuron-like spike (see Figure 1.25d). In particular, the hyperpotential (part d) arises from the battery potential of M_2 memristive device after removing external electric potential. The output spike frequency is tunable through control of the input signals, as given in Figure 1.25e, and it is found that the interaction of protons and electrons in M_2 resembles the coordination of K^+ and Na^+ ion channels in the neuron membrane. To the best of our knowledge, this is the first physical demonstration of artificial neurons with functions described in both biophysical and bioplausible neuron models.

In these years, memristor has been intensively investigated for the construction of artificial synapses and neurons because of its simple structure and rich dynamics. In this chapter, we first briefly introduce the state-of-art memristive synapses including short-term memristive synapses and long-term memristive synapses. Subsequently, recently reported memristive neurons, such as bioplausible neurons and biophysical neurons, are discussed. Here, bioplausible neurons consist of IF neurons and LIF neurons, and biophysical neurons refer to HH neurons.

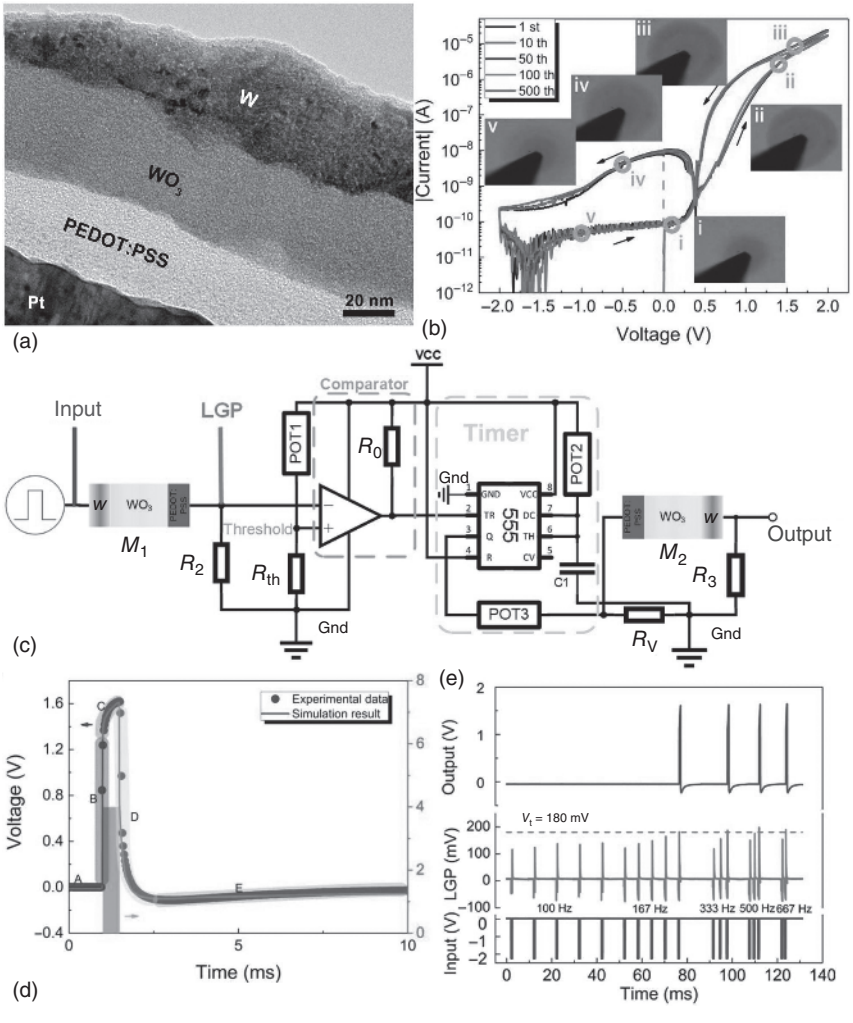

Figure 1.25 HH neuron with LIF functions. (a) The cross-sectional TEM image of the W/WO_3/PEDOT:PSS/Pt device. (b) *I–V* curves of the analog switching. (c) Electrical circuit of the proposed HH neuron with two W/WO_3/PEDOT:PSS/Pt memristive devices. The first memristive device handles the tasks of integration and leaky, while the second one is used to realize the fire function. (d) Experimental and simulation results of the firing spike, which is in good agreement with biological spikes. (e) Temporal integration and bioinspired fire realized with the circuit. Source: (b–e) Huang et al. [10].

1.4 Memristive Neural Networks

1.4.1 Memristive ANN Computing

Two training approaches have been proposed to realize memristive ANN computing, offline training, and online training. In the case of offline training, the training

process is done by software with the memristive device model. Then, the obtained synaptic weight is mapped into the memristive device crossbar. The salient features of quickly parallel operation in memristive device crossbar will accelerate the working process of networks. In contrast, in online training approach, the training process is directly done on the memristive device crossbar, which enables parallel operation in both training and working processes.

In 2017, Sheridan et al. [143] implemented sparse coding algorithms in a 32×32 crossbar array of WO_x analog memristive devices, as shown in Figure 1.26a. This memristive network was offline trained by software; the obtained synaptic weight was then mapped to synaptic crossbar array via controlling the input pulse duration. The reconstructed image composed of the individual patches based on sparse-coding algorithm reproduces the original image well; see Figure 1.26b. Actually, this offline training approach is compatible with almost all algorithms used in ANNs; thus neural networks with different goals can be built in this way. In 2018, Hu and his coworkers [144] demonstrated a 128×64 one-transistor-one-memristive device (1T1M) array and achieved an 89.9% recognition accuracy for 10 000 Modified National Institute of Standards and Technology (MNIST) handwritten digit test set in a single-layer neural network, as shown in Figure 1.26c,d. Very recently, long short-term memory networks have been developed based on the same 128×64 1T1M array, with which predicting airline passenger numbers and identifying an individual human-based gait were successfully realized [151]. They then combined the convolutional neural networks (CNN) with LSTM networks to demonstrate the ConvLSTM, which classifying the MNIST-sequence videos [152].

Unlike offline training, online training approach means most of the training computation works are directly done on the memristive device crossbar. Moreover, the online learning self-adaptively mitigated the impact of the hardware imperfections [152]. In 2015, Prezioso et al. [145] developed a single-layer perceptron using 10×6 fragment of the TiO_{2-x} memristive device crossbar array; see Figure 1.26e. This network was online trained using the Manhattan update rule, i.e. a coarse–grain variety of delta rule, to perform the classification of 3×3-pixel black/white image into three classes (Figure 1.26f). It is found that Manhattan update rule is more feasible for the online training in memristive device crossbars, as given in Figure 1.26g. In 2017, Yao and his coworkers [146] experimentally demonstrated a 128×8 1T1M array and realized gray-scale face classification through parallel online training based on Manhattan update rule; see Figure 1.26h. In addition to Manhattan update rule, Sanger's rule can also be used to update synaptic weight to realize principal component analysis in memristive networks with 9×2 TaO_x array [147] (see Figure 1.26i). Compared with single-layer networks, multilayer networks are generally much more powerful in defects tolerance, as shown in Figure 1.26j. That is because the hidden neurons are helpful for minimizing the impact of device defects. Bayat et al. [153] experimentally demonstrated a multilayer memristive networks composed of two 20×20 transistor-free crossbar arrays and realized classification of letters. Li and his coworkers [148] demonstrated a multilayer network composed of 128×54 array for the first layer and 108×10 array for the second layer. They achieved much higher accuracy (91.7%) than the single layer networks (89.9%) [144] on the MNIST

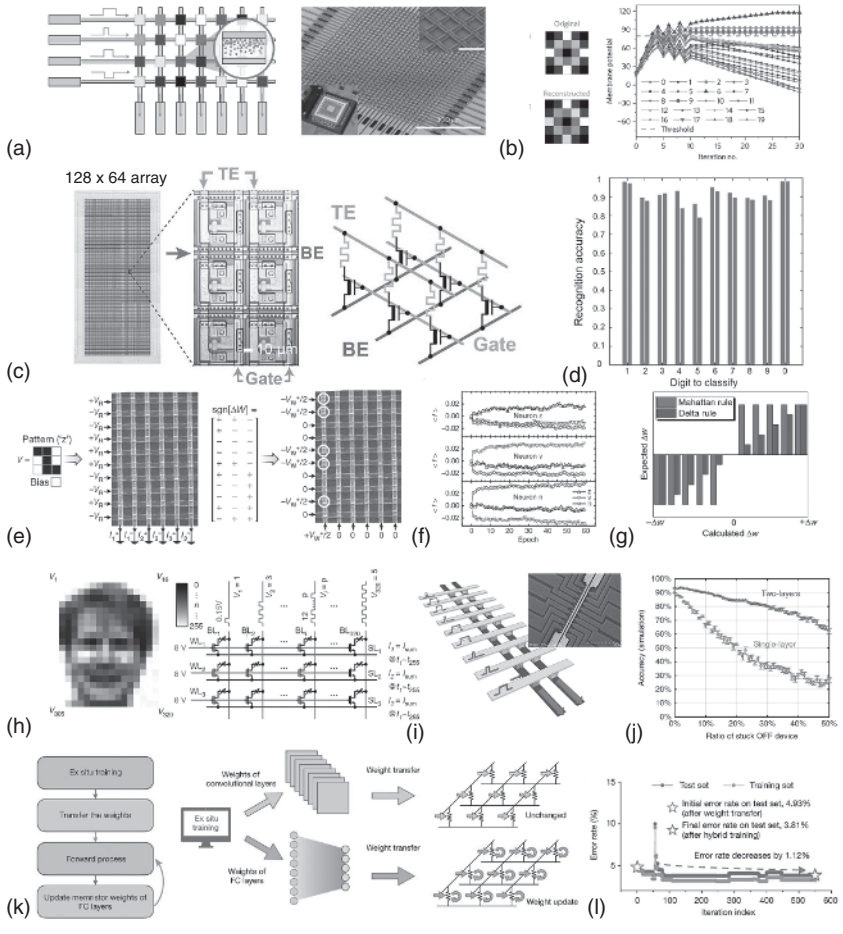

Figure 1.26 Memristive ANN computing. (a) Left: Schematic of a memristive device crossbar-based computing system, showing the input neurons (the left), the memristive device crossbar array, and the output neurons (the bottom). A memristive device is formed at each cross-point and can be programmed to different conductance states. Right: Scanning electron micrograph (SEM) image of a fabricated 32×32 WO_x memristive device array. (b) The original image and the reconstructed image based on sparse coding in the memristive device networks. The membrane potentials of the neurons as a function of iteration number during locally competitive algorithm (LCA) analysis. Source: (a, b) Sheridan et al. [143]. (c) The fabricated 128×64 1T1M memristive device array. (d) Total recognition accuracy for each digit for 10 000 images from the MNIST database based on the128×64 1T1M memristive device array. Source: (c, d) Hu et al. [144]. (e) The fabricated 10×6 TiO_{2-x} memristive device array without transistors. (f) The evolution of output signals in this 10×6 TiO_{2-x} memristive device array, averaged over all patterns of a specific class. Source: (e, f) Prezioso et al. [145]. (g) The Manhattan rule and delta rule show different Δw in the same calculated Δw. The sign is the only parameter considered in the Manhattan rule, while the amplitude is also included in the delta rule. (h) The schematic of parallel read operation and how a pattern is mapped to the input in the 128×8 1T1M array for face classification [146]. (i) Schematic diagram and SEM image of a 2×9 memristive device array for principal component analysis. Source: Choi et al. [147]. (j) The multilayer network helps with defect tolerance. If one device is stuck, the associated hidden neuron will adjust the connections accordingly Source: Li et al. [148]. (k) Schematic diagram of hybrid trained method. Source: Yao et al. [149]. (l) Error-rate traces over 550 hybrid training iteration cycles. Source: Based on Cai et al. [150].

handwritten recognition. Wang et al. [154] realized a reinforcement learning on a three-layer network and performed two control problems of the cart-pole and mountain car simulations.

Recently, a new hybrid training method is put forward, including the offline trained weights of the convolutional kernel and the online trained weights of the full connected layer. Yao and his coworkers [149] firstly implemented a memristor-based CNN with the fully hardware. They achieve a high accuracy (>96%) for MNIST handwritten digits by utilizing hybrid training (as shown in Figure 1.26k) to accommodate nonideal device characteristics and accelerate the process by parallel computing. In addition, the energy efficiency is much greater (more than 2 orders of magnitude) than that of state-of-the-art graphics processing. Cai et al. [150] integrated a passive crossbar array with traditional CMOS circuits (Figure 1.26l), including a full set of mixed-signal interface blocks and a computing processer based on digit computing. The integrated system provided the hardware solutions for neural networks with high speed and efficient power consumption.

1.4.2 Memristive SNN Computing

In comparison with memristive ANN networks, the progress on memristive SNN networks is quite limited due to the lack of mature algorithms and comparable simple circuits for SNN. Even so, some encouraging breakthroughs have been made in memristive SNN computing. In 2015, Nishitani and his coworkers [155] proposed a supervised learning model with simplified error backpropagation in a memristive SNN, in which a three-terminal ferroelectric memristive device functions as synapses to store analog synaptic weight. In this spiking backpropagation method, the input signal and output signal are all spiking timing. Also, the synaptic weight update process is divided into two steps. In the first step, only the output layer is updated, whereas in the second step, both output layer and hidden layer were updated. When the output spikes approach the desired timing, the residual error rapidly drops, meaning that the supervised learning process succeeded. Li and his coworkers [156] applied the volatile device to emulate the forgetting phenomenon of the biological brain. In the training procedure, the potentiation and forgetting of the synaptic weights are realized based on the electric pulses and the time intervals, respectively. Recently, Wang and his coworkers [131] developed a prototypical integrated capacitive switching neural network and realized associative learning and signal classification, as shown in Figure 1.27a–c. In their prototypical networks, neurons are represented by a pseudo-memcapacitor composed of a volatile diffusive memristive device and a series capacitor (Figure 1.27a), and the synapses share the similar structure with neurons but using a nonvolatile memristive device to replace the volatile diffusive memristive devices.

In addition to supervised learning, unsupervised learning has also been experimentally implemented in memristive SNN. In 2016, Serb et al. [157] experimentally realized weight-dependent STDP in the TiO_{2-x} memristive devices; see Figure 1.27d. Then, they demonstrated unsupervised learning in a prototype probabilistic neural network (Figure 1.27e), in which four input synapses are implemented by hardware

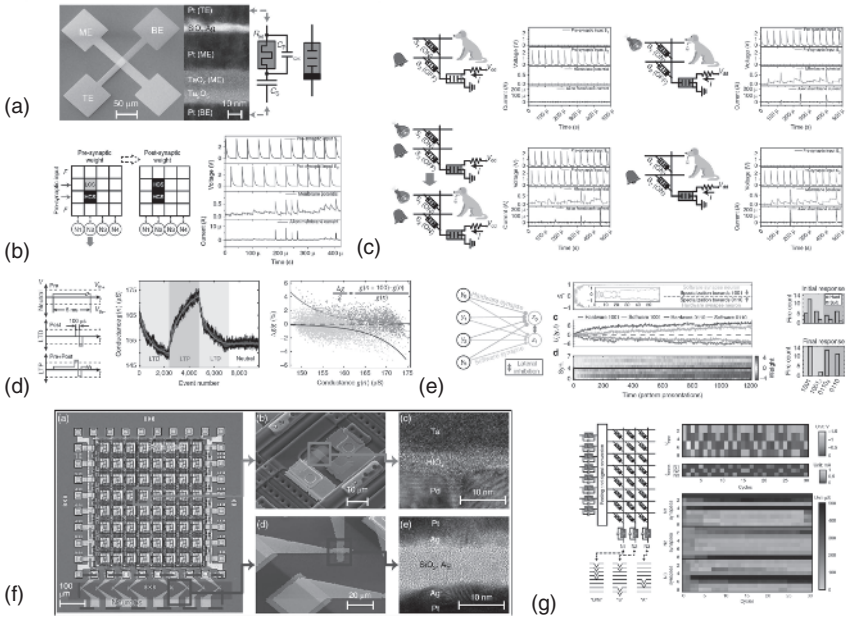

Figure 1.27 Memristive SNN computing. (a) Scanning electron micrograph of the plan view of the integrated dynamic pseudo-memcapacitor composed of a volatile diffusive memristive device and a series capacitor and a transmission electron micrograph of the cross section. (b) Schematic illustration and experimental observation of the synapse programming using the Hebbian-like mechanism. Simultaneous presynaptic signals (dark gray and light lines in ii) were applied to both the low capacitance state (LCS) synapse and the high capacitance state (HCS) synapse. (c) Capacitive network for associative learning based on the Hebbian-like mechanism. Two presynaptic signals model the sight of food and the sound of a bell, respectively. The postsynaptic neuron models the salivation of a dog. Source: (a–c) Wang et al. [131]. (d) Weight-dependent STDP in the TiO_{2-x} memristive devices. (e Unsupervised learning in a winner-take-all network with a mixture of software and memristive device synapses. Source: (d, e) Serb et al. [157]. (f) All memristive neural network, consisting of an 8×8 1T1R memristive synapse crossbar interfacing with eight diffusive memristive device artificial neurons. (g) Unsupervised training of an all-memristive neural network based on STDP learning rules. Source: (f, g) Wang et al. [129].

TiO_{2-x} memristive devices while the other four synapses are implemented by software. The final classification results are optimized when enough unlabeled inputs are feed in the networks through the introduction of probabilistic in the trigger conditions of neurons. Moreover, successful learning can be achieved, even if there are corrupted inputs. Wang et al. [129] recently built a fully memristive neural network, in which the LIF neurons composed of a diffusive memristive device and a parallel capacitor were directly connected with the memristive 1T1M arrays, as shown in Figure 1.27f. This fully memristive network is capable of performing unsupervised learning using STDP learning rule for pattern classification. Software pooling and signal conversion are used to convert the Rectified Linear Units (ReLUs) layer output to timing signals. Then these signals acting as inputs are fed into the fully connected layer using STDP rules; see Figure 1.27g. This is an important step toward

the hardware implementation of all memristive spiking neural networks sharing extremely similar neuron and synaptic dynamics to their biological counterparts. As for trained methods for unsupervised SNN, Guo and his coworkers [158] utilized the STDP as the learning rule and proposed to dilute spike events in encoding the input data, endowing the networks with the ability of working with the large conductance variations of the synaptic devices.

In the last, we briefly introduce the state-of-art memristive neural networks in the final section, including offline/online training in memristive crossbar for ANN and supervised/unsupervised learning achieved in memristive SNN.

1.5 Summary and Outlook

In this chapter, we have given an overview on two-terminal neuromorphic memristors used in brain-inspired computing. The device structure, materials, resistive switching behaviors, and mechanisms are presented considering unique requirements for neuromorphic computing. Furthermore, state-of-art demonstrations of memristive synapses, neurons, and corresponding neural networks including ANN and SNN have been discussed in detail. Despite encouraging progresses have been achieved in last few decades, memristor-based brain-inspired computing is still in its infancy, and there are many challenges to be resolved at both device level and system level.

At the device level, an ideal synaptic element combining high yield, superior stability, and small cycle-to-cycle and device-to-device variations is still unavailable, which is obstacle for maximizing the computing accuracy of offline training memristive systems. This is because the switching mechanisms of most memristive synapses are based on metal or oxygen ions migration, leading to the stochastic formation/rupture of conductive filaments. This inevitably induces low yield and large variations. Therefore, considerable efforts should be devoted to explore new switching mechanisms with high controllability and reliability. Furthermore, high linearity and symmetry of the conductance modulation are key parameters in maximizing the accuracy in online training networks. However, most reported memristive synapses show large nonlinearity and asymmetry. To address this issue, further device engineering is needed, and co-optimization studies between devices, algorithms, and circuits might also be necessary. For memristive neurons, the exploration of some dynamic physicochemical processes in memristive devices to faithfully reproduce the neuron dynamics is required for the implementation of all memristive bioinspired computing.

At the system level, the sneak current, which flows through unselected cells, can severely restricts the size of synapse array. Although the 1T1M configuration can effectively address the sneak path problem, the additional three-terminal transistors will remarkably increase the circuit complexity and affect the integration density of crossbar arrays. Fortunately, memristive synapses with nonlinear or self-rectifying switching behavior are preferable for the construction of transistor-free crossbar arrays. In addition, the learning algorithms of memristive ANN and SNN are still

under development. Therefore, it is necessary to develop new network topology and learning algorithms that are prevalent for memristive ANN and SNN, in particular those that can take advantage of the unique properties of memristors.

Last but not the least, close collaboration between materials scientists, computer architects, and neuroscientists is crucial to demonstrate large-scale memristive bioinspired computing systems for practical applications.

References

1 Chua, L.O. (1971). *IEEE Trans. Circuit Theory* 18: 507.
2 Strukov, D.B., Snider, G.S., Stewart, D.R., and Williams, R.S. (2008). *Nature* 453: 80.
3 Jeong, D.S., Thomas, R., Katiyar, R.S. et al. (2012). *Rep. Prog. Phys.* 75: 076502.
4 Sawa, A. (2008). *Mater. Today* 11: 28.
5 Gao, S., Zeng, F., Chen, C. et al. (2013). *Nanotechnology* 24: 335201.
6 Gao, S., Song, C., Chen, C. et al. (2012). *J. Phys. Chem. C* 116: 17955.
7 Chen, C., Yang, Y.C., Zeng, F., and Pan, F. (2010). *Appl. Phys. Lett.* 97: 083502.
8 Peng, C.N., Wang, C.W., Chan, T.C. et al. (2012). *Nanoscale Res. Lett.* 7: 559.
9 Ma, L.P., Liu, J., and Yang, Y. (2002). *Appl. Phys. Lett.* 80: 2997.
10 Huang, H.-M., Yang, R., Tan, Z.-H. et al. (2018). *Adv. Mater.*: 1803849.
11 Lee, M.-J., Lee, D., Cho, S.-H. et al. (2013). *Nat. Commun.* 4: 2629.
12 Son, J.Y., Shin, Y.-H., Kim, H., and Jang, H.M. (2010). *ACS Nano* 4: 2655.
13 Tsai, C.-L., Xiong, F., Pop, E., and Shim, M. (2013). *ACS Nano* 7: 5360.
14 Hu, D.-C., Yang, R., Jiang, L., and Guo, X. (2018). *ACS Appl. Mater. Interfaces* 10: 6463.
15 Moors, M., Adepalli, K.K., Lu, Q.Y. et al. (2016). *ACS Nano* 10: 1481.
16 Tang, G.S., Zeng, F., Chen, C. et al. (2013). *J. Appl. Phys.* 113: 244502.
17 Yang, Y., Gao, P., Li, L. et al. (2014). *Nat. Commun.* 5: 4232.
18 Wang, D.T., Dai, Y.W., Xu, J. et al. (2016). *IEEE Electron Device Lett.* 37: 878.
19 Hong, D.S., Chen, Y.S., Sun, J.R., and Shen, B.G. (2016). *Adv. Electron. Mater.* 2: 1500359.
20 Jiang, J., Guo, J.J., Wan, X. et al. (2017). *Small* 13: 1700933.
21 Yin, X.B., Tian, K., Tan, Z.H. et al. (2015). *J. Electrochem. Soc.* 162: 271.
22 Lee, M.-J., Lee, C.B., Lee, D. et al. (2011). *Nat. Mater.* 10: 625.
23 Kumar, S., Wang, Z., Huang, X. et al. (2016). *ACS Nano* 10: 11205.
24 Tan, Z.H., Yang, R., Terabe, K. et al. (2016). *Adv. Mater.* 28: 377.
25 Yang, R., Huang, H.M., Hong, Q.H. et al. (2018). *Adv. Funct. Mater.* 28: 1704455.
26 Shi, T., Yang, R., and Guo, X. (2016). *Solid State Ionics* 296: 114.
27 Jeong, H.Y., Kim, J.Y., Kim, J.W. et al. (2010). *Nano Lett.* 10: 4381.
28 Shi, Y., Liang, X., Yuan, B. et al. (2018). *Nat. Electron.* 1: 458.
29 Wu, Y., Lee, B., and Philip Wong, H.-S. (2010). *IEEE Electron Dev. Lett.* 31: 1449.
30 Du, C., Ma, W., Chang, T. et al. (2015). *Adv. Funct. Mater.* 25: 4290.

31 Yin, X.-B., Tan, Z.-H., and Guo, X. (2015). *Phys. Chem. Chem. Phys.* 17: 134.
32 Tan, Z.-H., Yin, X.-B., Yang, R. et al. (2017). *Sci. Rep.* 7: 713.
33 Tian, H., Mi, W.T., Zhao, H.M. et al. (2017). *Nanoscale* 9: 9275.
34 Kostarelos, K. and Novoselov, K.S. (2014). *Nat. Nanotechnol.* 9: 744.
35 Wang, Q.H., Zadeh, K.K., Kis, A. et al. (2012). *Nat. Nanotechnol.* 7: 699.
36 Bessonov, A.A., Kirikova, M.N., Petukhov, D.I. et al. (2015). *Nat. Mater.* 14: 199.
37 Cheng, P., Sun, K., and Hu, Y.H. (2016). *Nano Lett.* 16: 572.
38 Wang, M., Cai, S., Pan, C. et al. (2018). *Nat. Electron.* 1: 130.
39 Novoselov, K.S., Jiang, D., Schedin, F. et al. (2005). *Proc. Natl. Acad. Sci.* 102: 10451.
40 Coleman, J.N., Lotya, M., O'Neill, A. et al. (2011). *Science* 331: 568.
41 Li, X.S., Cai, W.W., An, J.H. et al. (2009). *Science* 324: 1312.
42 Eda, G., Yamaguch, H., Voiry, D. et al. (2011). *Nano Lett.* 11: 5111.
43 Chen, Y., Liu, G., Wang, C. et al. (2014). *Mater. Horiz.* 1: 489.
44 Wang, Z.S., Zeng, F., Yang, J. et al. (2010). *Appl. Phys. Lett.* 97: 253301.
45 Yang, J., Zeng, F., Wang, Z.S. et al. (2011). *J. Appl. Phys.* 110: 114518.
46 Son, D.I., Kim, T.W., Shim, J.H. et al. (2010). *Nano Lett.* 10: 2441.
47 Yang, R., Huang, H.M., and Guo, X. (2019). *Adv. Electron. Mater.* 5: 1900287.
48 Pan, F., Gao, S., Chen, C. et al. (2014). *Mater. Sci. Eng. R-Rep* 83: 1.
49 Waser, R., Dittmann, R., Staikov, G., and Szot, K. (2009). *Adv. Mater.* 21: 2632.
50 Wang, J. and Zhuge, F. (2019). *Adv. Mater. Technol.* 4: 1800544.
51 Sawa, A., Fujii, T., Kawasaki, M., and Tokura, Y. (2004). *Appl. Phys. Lett.* 85: 4073.
52 Wang, Z., Joshi, S., Savel'ev, S.E. et al. (2017). *Nat. Mater.* 16: 101.
53 Jo, S.H., Chang, T., Ebong, I. et al. (2010). *Nano Lett.* 10: 1297.
54 Shi, Y., Nguyen, L., Oh, S. et al. (2018). *Nat. Commun.* 9: 5312.
55 Zidan, M.A., Strachan, J.P., and Lu, W.D. (2018). *Nat. Electron.* 1: 22.
56 Yu, S.M. (2018). *Proc. IEEE* 106: 260.
57 Yang, J.J., Miao, F., Pickett, M.D. et al. (2009). *Nanotechnology* 20: 215201.
58 Kim, S.G., Han, J.S., Kim, H. et al. (2018). *Adv. Mater. Technol.* 3: 1800457.
59 Valov, I., Waser, R., Jameson, J.R., and Kozicki, M.N. (2011). *Nanotechnology* 22: 254003.
60 Lu, W., Jeong, D.S., Kozicki, M., and Waser, R. (2012). *Mater. Res. Soc. Bull.* 37: 124.
61 Hasegawa, T., Terabe, K., Tsuruoka, T., and Aono, M. (2012). *Adv. Mater.* 24: 252.
62 Yang, Y. and Lu, W. (2013). *Nanoscale* 5: 10076.
63 Hirose, Y. and Hirose, H. (1976). *J. Appl. Phys.* 47: 2767.
64 Zidan, M.A., Chen, A., Indiveri, G., and Lu, W.D. (2017). *J. Electroceram.* 39: 4.
65 Yang, Y., Gao, P., Gaba, S. et al. (2012). *Nat. Commun.* 3: 732.
66 Yang, Y., Gao, P., Li, L. et al. (2014). *Nat. Commun.* 5: 2382.
67 Choi, S.-J., Park, G.-S., Kim, K.-H. et al. (2011). *Adv. Mater.* 23: 3272.
68 Kwon, D.-H., Kim, K.M., Jang, J.H. et al. (2010). *Nat. Nanotechnol.* 5: 148.
69 Strachan, J.P., Pickett, M.D., Yang, J.J. et al. (2010). *Adv. Mater.* 22: 3573.
70 Kumar, S., Graves, C.E., Strachan, J.P. et al. (2016). *Adv. Mater.* 28: 2772.

71 Baeumer, C., Schmitz, C., Ramadan, A.H.H. et al. (2015). *Nat. Commun.* 6: 8610.

72 Baeumer, C., Raab, N., Menke, T. et al. (2016). *Nanoscale* 8: 13967.

73 Bagdzevicius, S., Maas, K., Boudard, M., and Burriel, M. (2017). *J. Electroceram.* 39: 157.

74 Hansen, M., Ziegler, M., Kolberg, L. et al. (2015). *Sci. Rep.* 5: 13753.

75 Yang, R., Terabe, K., Liu, G. et al. (2012). *ACS Nano* 6: 9515.

76 Zhou, W., Yang, R., He, H.-K. et al. (2018). *Appl. Phys. Lett.* 113: 061107.

77 Mikheev, E., Hoskins, B.D., Strukov, D.B., and Stemmer, S. (2014). *Nat. Commun.* 5: 3990.

78 Arndt, B., Borgatti, F., Offi, F. et al. (2017). *Adv. Funct. Mater.* 27: 1702282.

79 Wang, Z.Q., Xu, H.Y., Li, X.H. et al. (2012). *Adv. Funct. Mater.* 22: 2759.

80 Ha, S.D. and Ramanathan, S. (2011). *J. Appl. Phys.* 110: 071101.

81 Asanuma, S., Akoh, H., Yamada, H., and Sawa, A. (2009). *Phys. Rev. B.* 80: 235113.

82 Lee, H.S., Park, H.H., and Rozenberg, M.J. (2015). *Nanoscale* 7: 6444.

83 Versace, M. and Chandler, B. (2010). *IEEE Spectrum* 47: 30.

84 Strukov, D.B. (2011). *Nature* 476: 403.

85 Thomas, A. (2013). *J. Phys. D Appl. Phys.* 46: 093001.

86 Mead, C.A. (1990). *Proc. IEEE* 78: 1629.

87 Ma, W., Zidan, M.A., and Lu, W.D. (2018). *Sci. China Inform. Sci.* 61: 060422.

88 Thomas, A. (2018). *Nat. Electron.* 1: 261.

89 John, R.A., Liu, F., Chien, N.A. et al. (2018). *Adv. Mater.* 30: 1800220.

90 Kirkwood, A., Rioult, M.G., and Bear, M.F. (1996). *Nature* 381: 526.

91 Nicholls, J.G., Martin, A.R., Fuchs, P.A. et al. (2012). *From Neuron to Brain*. Sunderland, MA: Sinauer Associates.

92 Debanne, D., Guerineau, N.C., Gähwiler, B., and Thompson, S.M. (1996). *J. Physiol.* 491: 163.

93 Waldeck, R.F., Pereda, A., and Faber, D.S. (2000). *J. Neurosci.* 20: 5312.

94 Atluri and Regehr, W.G. (1996). *J. Neurosci.* 16: 5661.

95 Kirischuk, S., Clements, J.D., and Grantyn, R. (2002). *J. Physiol.* 543: 99.

96 Zhu, L.Q., Wan, C.J., Guo, L.Q. et al. (2014). *Nat. Commun.* 5: 3158.

97 Xu, W., Cho, H., Kim, Y.H. et al. (2016). *Adv. Mater.* 28: 5916.

98 Li, B., Liu, Y., Wan, C. et al. (2018). *Adv. Mater.* 30: 1706395.

99 Milano, G., Luebben, M., Ma, Z. et al. (2018). *Nat. Commun.* 9: 5151.

100 Najem, J.S., Taylor, G.J., Weiss, R.J. et al. (2018). *ACS Nano* 12: 4702.

101 Zhang, Y., Zhong, S., Song, L. et al. (2018). *Appl. Phys. Lett.* 113: 203102.

102 Raymond, C.R. and Redman, S.J. (2006). *J. Physiol.* 570: 97.

103 Froemke, R.C. and Dan, Y. (2002). *Nature* 416: 433.

104 Raymond, C.R. (2007). *Trends Neurosci.* 30: 167.

105 Bear, M.F. and Malenka, R.C. (1994). *Curr. Opin. Neurobiol.* 4: 389.

106 Bienenstock, E.L., Cooper, L.N., and Munro, P.W. (1982). *J. Neurosci.* 2: 32.

107 Benuskova, L., Diamond, M.E., and Ebner, F.F. (1994). *Proc. Natl. Acad. Sci. U. S. A.* 91: 4791.

108 Serrano-Gotarredona, T., Masquelier, T., Prodromakis, T. et al. (2013). *Front. Neurosci.* 7: 2.

109 Abbott, L.F. and Nelson, S.B. (2000). *Nat. Neurosci.* 3: 1178.

110 Prezioso, M., Merrikh Bayat, F., Hoskins, B. et al. (2016). *Sci. Rep.* 6: 21331.

111 Kuzum, D., Jeyasingh, R.G.D., Lee, B., and Wong, H.S.P. (2012). *Nano Lett.* 12: 2179.

112 Alibart, F., Pleutin, S., Bichler, O. et al. (2012). *Adv. Funct. Mater.* 22: 609.

113 Li, Y., Zhong, Y.P., Zhang, J.J. et al. (2014). *Sci. Rep.* 4: 4906.

114 Kim, S., Choi, S., Lee, J., and Lu, W.D. (2014). *ACS Nano* 8: 10262.

115 He, W., Huang, K.J., Ning, N. et al. (2014). *Sci. Rep.* 4: 4755.

116 Rubin, J.E., Gerkin, R.C., Bi, G.Q., and Chow, C.C. (2005). *J. Neurophysiol.* 93: 2600.

117 Kim, S., Du, C., Sheridan, P. et al. (2015). *Nano Lett.* 15: 2203.

118 Xiong, J., Yang, R., Shaibo, J. et al. (2019). *Adv. Funct. Mater.*: 1807316.

119 Sokolov, A.S., Jeon, Y.-R., Kim, S. et al. (2019). *NPG Asia Mater.* 11: 5.

120 Yi, W., Tsang, K.K., Lam, S.K. et al. (2018). *E. A. J. N. c. Flores, Nat. Commun.* 9: 4661.

121 Gerstner, W. and Naud, R. (2009). *Science* 326: 379.

122 Bao, L., Kang, J., Fang, Y.C. et al. (2018). *Sci. Rep.* 8: 13727.

123 Pickett, M.D., Medeiros-Ribeiro, G., and Williams, R.S. (2012). *Nat. Mater.* 12: 114.

124 Tuma, T., Pantazi, A., Le Gallo, M. et al. (2016). *Nat. Nanotechnol.* 11: 693.

125 Ziegler, M., Wenger, C., Chicca, E., and Kohlstedt, H. (2018). *J. Appl. Phys.* 124: 152003.

126 Amirsoleimani, A., Ahmadi, M., and Ahmadi, A. (2017). Presented at the 2017 International Joint Conference on Neural Networks, Anchorage, AK, May.

127 Bao, H., Liu, W., and Hu, A. (2019). *Nonlinear Dyn.* 95: 43.

128 Nicholls, J.G., Martin, A.R., Wallace, B.G., and Fuchs, P.A. (2001). *From Neuron to Brain*. Sunderland, MA: Sinauer Associates.

129 Wang, Z., Joshi, S., Savel'ev, S. et al. (2018). *Nat. Electron.* 1: 137.

130 Zhang, X., Wang, W., Liu, Q. et al. (2018). *IEEE Electron Device Lett.* 39: 308.

131 Wang, Z., Rao, M., Han, J.-W. et al. (2018). *Nat. Commun.* 9: 3208.

132 Stoliar, P., Tranchant, J., Corraze, B. et al. (2017). *Adv. Funct. Mater.* 27: 1604740.

133 Zhang, Y., He, W., Wu, Y. et al. (2018). *Small* 14: 1802188.

134 Yi, W., Tsang, K.K., Lam, S.K. et al. (2018). *Nat. Commun.* 9: 4661.

135 Lim, H., Kornijcuk, V., Seok, J.Y. et al. (2015). *Sci. Rep.* 5: 9776.

136 Ignatov, M., Ziegler, M., Hansen, M. et al. (2015). *Front. Neurosci.* 9: 376.

137 Feali, M.S., Ahmadi, A., and Hayati, M. (2018). *Neurocomputing* 309: 157.

138 Mehonic, A. and Kenyon, A.J. (2016). *Front. Neurosci.* 10: 57.

139 Agrawal, A. and Roy, K. (2019). *IEEE Trans. Magn.* 55: 1400107.

140 Chen, X., Kang, W., Zhu, D. et al. (2018). *Nanoscale* 10: 6139.

141 Mizrahi, A., Hirtzlin, T., Fukushima, A. et al. (2018). *Nat. Commun.* 9: 1533.

142 Feali, M.S. and Ahmadi, A. (2017). *Neural Processing Lett.* 45: 1.

143 Sheridan, P.M., Cai, F., Du, C. et al. (2017). *Nat. Nanotechnol.* 12: 784.

144 Hu, M., Graves, C.E., Li, C. et al. (2018). *Adv. Mater.* 30: 1705914.
145 Prezioso, M., Merrikh-Bayat, F., Hoskins, B.D. et al. (2015). *Nature* 521: 61.
146 Yao, P., Wu, H., Gao, B. et al. (2017). *Nat. Commun.* 8: 15199.
147 Choi, S., Shin, J.H., Lee, J. et al. (2017). *Nano Lett.* 17: 3113.
148 Li, C., Belkin, D., Li, Y. et al. (2018). *Nat. Commun.* 9: 2385.
149 Yao, P., Wu, H., Gao, B. et al. (2020). *Nature* 577: 641.
150 Cai, F., Correll, J.M., Lee, S.H. et al. (2019). *Nat. Electr.* 2: 290.
151 Li, C., Wang, Z., Rao, M. et al. (2019). *Nat. Mach. Intell.* 1: 49.
152 Wang, Z., Li, C., Lin, P. et al. (2019). *Nat. Mach. Intell.* 1: 434.
153 Bayat, F.M., Prezioso, M., Chakrabarti, B. et al. (2018). *Nat. Commun.* 9: 2331.
154 Wang, Z., Li, C., Song, W. et al. (2019). *Nat. Electr.* 2: 115.
155 Nishitani, Y., Kaneko, Y., and Ueda, M. (2015). *IEEE Trans. Neural Netw. Learn. Syst.* 26: 2999.
156 Li, J., Xu, H., Sun, S.-Y. et al. (2020). *Neurocomputing* 408: 21.
157 Serb, A., Bill, J., Khiat, A. et al. (2016). *Nat. Commun.* 7: 12611.
158 Guo, Y., Wu, H., Gao, B., and Qian, H. (2019). *Frontiers in Neuroscience*: 13.